Title: Ongoing oversanding induces biological soil crust layering – a new approach for biological soil crust structure elucidation determined from high resolution penetration resistance data

Vincent J. M. N. L. Felde[1,2], Sylvie L. Drahorad[1], Peter Felix-Henningsen[1], Stephen R. Hoon[3]

[1]Institute of Soil Science and Soil Conservation, Research Centre for Biosystems, Land Use and Nutrition (IFZ), Justus Liebig University, Heinrich-Buff-Ring 26-32, 35392 Giessen, Germany

[2]Department of Soil Science, University of Kassel, Nordbahnhofstr. 1A, 37213 Witzenhausen, Germany

[3]School of Science and the Environment, Manchester Metropolitan University, Chester St., Manchester, M1 5GD, UK

Corresponding author: Vincent J. M. N. L. Felde

Tel.: +49-561-804-1664, FAX: +49-561-804-1590

E-mail: felde@uni-kassel.de

Keywords: Negev desert; electronic micro penetrometer; micro layering; sand soil; desertification

Abstract

The aim of this study was to determine the *in-situ* strength and microscopic characteristics of bio-physical micro-horizons in the top 40 mm of oversanded sand soils detected by depth dependent penetration resistance (PR). These micro-horizons result from the burial of biological soils crust (BSC) surfaces and contribute to soil stability. They are also important as the biotic source for seeding new surficial crusts. *Ex-situ* polarised optical micrograph was employed to determine the bio-physical structures associated with the fossil BSC horizons. An automated electronic micro penetrometer (EMP) determining *in-situ* depth dependent soil PR was used for the quantitative detection of surface and buried micro-horizons. PR data was modelled using a multi-component / soil and micro-horizon multilayer plastic shear stress model. This enabled determination of soil and sediment structure, the contribution of buried 'fossil' BSCs to soil strength and structural mapping. We also employed proxy (synthetic) layered soil systems to determine the effect of EMP shaft and probe tip shape upon the PR profile. This methodology represents a significant improvement over penetrometer methods that only use single-value surface breaking point information. We find that buried BSC structures can contribute over 80 % of the soil strength even at *ca*. 20 mm depth and that the strength of a buried crust, at least in the medium term, can exceed that of (developing) surficial ones. Typical soil strengths of BSCs in the Negev desert, Israel lie between 1.5 and 3.6 MPa. Finally we discuss the effects and potential importance that buried BSC horizons may have upon heat, and the percolation and diffusion of moisture and gas through structured bio-physical, BSC capped sand soil systems.

1. Introduction

Biological soil crusts (BSCs) cover large areas of dryland soils in arid and semiarid areas (Belnap et al., 2016) and are considered a key element in landscape stability (Jimenez Aguilar *et al.*, 2009). BSC organisms are able to grow under high light intensities and have developed various survival strategies in order to cope with harsh environmental conditions, such as frequent hydration and desiccation (Fierer *et al.*, 2003; Pócs, 2009; West, 1990). As drylands cover approximately 40 % of the global land surface and support 38 % of the human population (Reynolds *et al.*, 2007), BSC covered soils are of significance to soil-atmosphere coupling and hence, potentially, an important part of global climate change models (Elbert *et al.*, 2012; Thomas and Hoon, 2010). Although often no more than a few millimetres in thickness, BSCs inhibit wind erosion and are important in protection against land degradation (Belnap and Gillette, 1998; Rodríguez-Caballero *et al.*, 2013; Zhang *et al.*, 2006). A recent study by Lan *et al.* (2014) proves that the artificial introduction of BSCs can even facilitate the reversal of desertification. Apart from lichens and, in part, bryophytes, cyanobacterial strains are the principal biomass producers in many desert soils (Belnap *et al.*, 2003). Cyanobacteria during their growth excrete extracellular polymeric substances (EPSs), forming a polymeric matrix (Chen *et al.*, 2014), which in early stage crusts constitutes the main source for organic carbon in the soil (Mager, 2010). EPSs stabilise the soil surface (Hu *et al.*, 2003a) and foster pedogenic processes in young soils (Dümig *et al.*, 2014). Further, EPSs swell during hydration (Fischer *et al.*, 2010) and are able to capture deposited dust (Williams *et al.*, 2012). This dust accumulation and the input of salts also contributes significantly to BSC aggregation and stabilisation (Drahorad and Felix-Henningsen, 2013; Zaady and Offer, 2010). Recent studies show that the overall stability of BSCs is strongly linked to their development and environmental conditions, such as land use history and soil properties (Chamizo *et al.*, 2015). A complex symbiotic community exists within BSCs. Lichens, bryophytes, mycorrhiza, bacteria, algae, cyanobacteria and fungi, the binding of soil particles by EPS sheaths and a stratified grain structure all contribute to the strength of BSCs. This biological community results in a cohesive crust possessing structural and consequently deformational properties that are expected to differ from the matrix of the underlying host soil. The mechanical stability

of BSCs strengthens as their age, thickness and biomass increase. For the Negev desert, Israel, Kidron *et al.* (2010) observed an increase in strength with ongoing succession from 0.009 to 0.076 MPa. Guo *et al.* (2008) found an increase in penetration resistance from 0.108 MPa for physical crusts to 0.126 MPa and 0.165 MPa for algal and moss crusts, respectively, on a stabilised sand dune surface in Inner Mongolia, China. Thomas and Dougill (2007) found the penetration resistance (PR) to increase with crust succession from 0.055 to 0.147 MPa in the Kalahari Desert, Botswana. For BSCs in the Karoo desert, South Africa, Dojani et al. (2011) found the mean penetration resistance to be 0.206 MPa. For a semi-arid steppe in SE Spain, Maestre et al. (2002) report the maximum penetration resistance of BSCs to be 0.698 MPa. Chamizo *et al.* (2015) have measured the PR of different crust types at two study sites in SE Spain in wet and dry states, as well as before and after crust removal. They found that the PR varied from 0.149 to 0.310 MPa and that both soil moisture content, and disturbance had a major effect on crust stability. Although these values vary significantly (due to in part to differences in methodology), this wide range of PR values is proof for the high site and soil substrate dependency of crust stability. However, what all these measurements have in common is that they only provide information on the maximum surface PR. BSCs also possess a vertical stratigraphy with regard to their stability and composition that is dependent upon metabolic differences in the organisms involved (Drahorad and Felix-Henningsen, 2013; Hu *et al.*, 2003b; Kidron *et al.*, 1999). Several studies from different arid and semiarid regions describe the existence of a thin, biologically enriched topcrust and a partly indurated section below this crust, referred to here after as a subcrust (e.g. Lan *et al.*, 2012; Malam Issa *et al.*, 2009) extending to a depth no more than 50 mm below the surface. Williams *et al.* (2012) found two macro scale layers for BSCs of the Mojave Desert, USA, often separated by a lateral linear void. In addition to being caused by a higher degree of aggregation in the upper layer, this void is also related to a change in the pore system, i.e. the occurrence of vesicular pore structures. These vesicles can occur either within the subcrust or underneath the BSC as a fully developed vesicular horizon (designated Av). These pore systems have been found in both desert BSCs (Felde *et al.*, 2014) and temperate region physical soil crusts (Badorreck *et al.*, 2013). Some studies indicate that the subcrust and the underlying soil can contain old, oversanded crusts

(Drahorad and Felix-Henningsen, 2013; Felde *et al.*, 2014; Malam Issa *et al.*, 2009) resulting in crust layering. This crust layering can be the result of either horizontal or vertical recolonization after burial. Studies from China have shown, however, that if oversanding exceeds a critical threshold of 1 cm, it causes severe damage to crust organisms inhibiting their functionality (Rao *et al.*, 2012) and, importantly, these buried crusts are not able to regenerate but remain more or less as a stable relict. Consequently, the new surface has to be colonised horizontally by pioneer crust organisms from neighbouring unburied crusts. If a recolonization does not take place, these buried BSCs are prone to erosion, once they are re-exposed (Kidron et al., 2016). Less intense oversanding, however, may allow mobile BSC organisms such as *Microcoleus vaginatus* to move upwards (Garcia-Pichel and Pringault, 2001) and recolonise the new surface vertically, rather than horizontally (Belnap *et al.*, 2003), forming a new topcrust. Thus, in sandy semiarid and arid soils buried BSCs are of great importance for topsoil stability, nutrient storage and turnover (Drahorad *et al.*, 2013) as well as water storage and water redistribution (Felde *et al.*, 2014). The use of penetration resistance (PR) data from field penetrometers for soil and sediment structure analysis and structural mapping has been reported in other studies (e.g. Anderson *et al.*, 1980; Boon *et al.*, 2005; Grunwald *et al.,* 2001; van Herwijnen *et al.*, 2009; Olsen, 1990). The BSCs of the Negev desert have been studied for over three decades, resulting in a comparatively good understanding of many of their ecological roles. For example, numerous studies have shown their importance for the carbon and nitrogen cycle (Drahorad et al., 2013; Kidron et al., 2015a, 2015b; Russow et al., 2005; Wilske et al., 2008), as well as different hydrological processes, such as surface runoff, evaporation and hydrophobicity (Keck et al., 2016; Kidron and Tal, 2012; Yair et al., 2011) or their effect on annual and perennial plants (Almog and Yair, 2007; Kidron, 2014; Prasse and Bornkamm, 2000).

However, the effect of sand burial and the resulting buried crust structures on BSC properties is largely unknown. Hence, the aim of this study was to determine the strength of micro-horizons resulting from the burial of old BSC surfaces using an automated electronic micro penetrometer (EMP, for a detailed description see Drahorad and Felix-Henningsen, 2012) in order to better understand their role in overall crust stability. The particular advantage

of the automated EMP employed here is its ability to ensure constancy or equivalence of operation, in particular its uniform penetration rate (16 mm min^{-1} or 267 µm sec^{-1}) enabling variation in the driving force to be related to intrinsic soil yield stresses. This study is the first to combine high resolution PR data and modelling for detailed structural elucidation of BSCs at high resolution. In order, however, to be able to properly interpret variations in PR in terms of corresponding soil micro structure, a model relating PR to layering is required. Here we present a mathematical model developed to interpret and characterise PR profiles, small scale boundaries and compositional changes within BSC covered topsoils based on the premise that the strength of soils, specifically their plastic yield and depth dependent deformation stress, can be determined using a soil penetrometer. We present data determined by the EMP interpreted using this model. The occurrence and stability of buried BSCs and layers on sub millimetre length scales has been detected. Our measurements and field observations of PR show the importance of morphological layering to overall BSC function as discussed below.

2. Material and Methods

2.1. Study site and BSC sampling

All field measurements and the BSC sampling were made in March 2013 at the beginning of the dry season at the study area *Nizzana-south*, in the NW Negev, Israel within the field site of the Arid Ecosystem Research Center of the Hebrew University of Jerusalem (Figure 1).

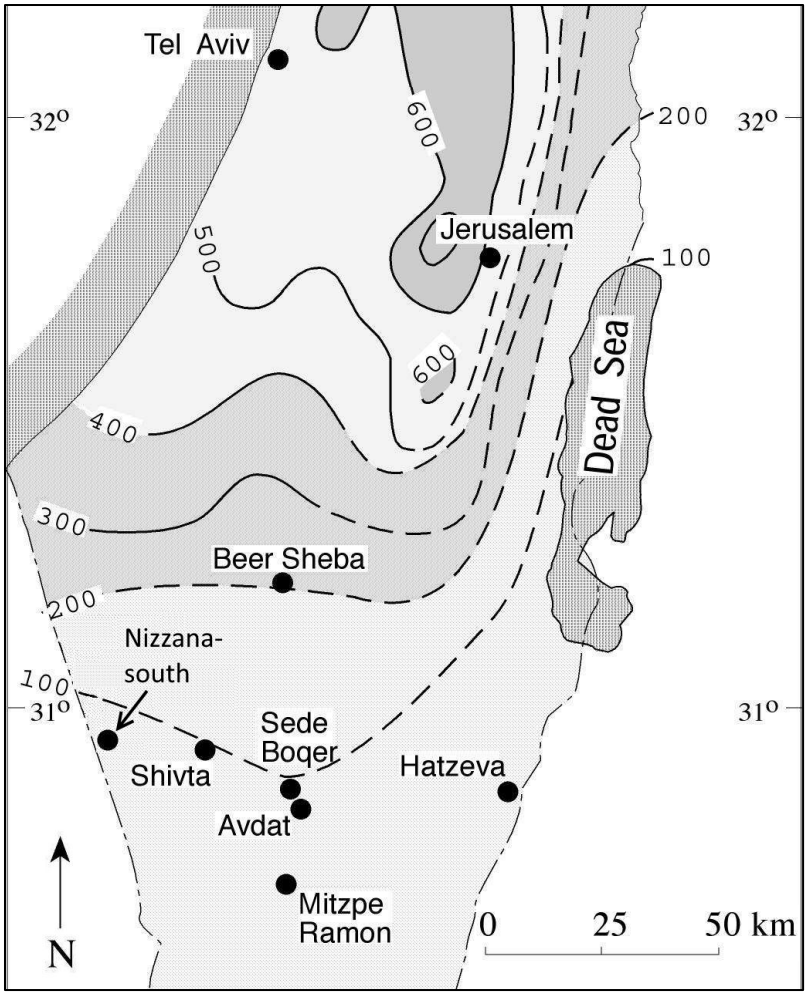

Figure 1: The study site, Nizzana-south located in the Nizzana sand dunes of the NW Negev, Israel. Isohyets with average annual rainfall, after Israel Meteorological Service The area is characterised by linear sand dunes, which are covered by BSCs on the dune flanks and in the interdunal valleys but possess uncrusted mobile dune crests due to high wind speeds preventing crust establishment (Kidron and Yair, 2008). The BSCs continue to undergo successional recovery as a consequence of land use exclusion since re-establishment of the

Egyptian-Israeli Sinai border in 1982 (Tsoar, 2008). The average annual rainfall is *ca.* 90 mm with high inter annual variations (Littmann and Berkowicz, 2008). The BSCs are dominated by cyanobacteria, such as *Trichocoleus sociatus*, *Microcoleus vaginatus*, *Scytonema sp.* and *Nostoc ssp*. (Büdel and Veste, 2008). For the characterization of BSC properties, 3 samples were taken randomly on south facing dune slopes within an area of approximately 3 square metres. Sampling of the soil was made at three depths; the active biological topcrust (0 – 2 mm), a more or less cemented subcrust at up to *ca.* 20 mm, and the topsoil to an absolute depth of 10 cm. In addition, the unconsolidated loose surface sand of the dune crest was sampled to serve as a proxy for uncrusted soil. All soil samples removed for *ex-situ* analysis in the laboratory were subsequently oven-dried (40 °C), sieved to 2 mm and partially finely ground (< 0.05 mm) for the determination of total nitrogen (N_t), total carbon (C_t), organic carbon (C_{org}) and calcium carbonate ($CaCO_3$) as described by Drahorad *et al.* (2013).

2.2. Thin sections and microscopic images of the soil proxies

Thin sections were prepared and analysed with a Keyence VHX-2000D optical microscope under transmission and cross-polarised light as described by Felde *et al.* (2014). Macroscopic features of the soil proxy material (see below) were observed at 5-200x and the microscopic characteristics of thin sections at 250-1500x. Images had a resolution of at least 1600x1200 pixels.

2.3. Soil proxy materials

Idealised soil proxy systems were built from proprietary rigid low density polyurethane and resol™ friable florist's foams in order to test the reproducibility of the EMP results, compare the behaviour of the different probe and shaft geometries, and, the ability of the mathematical model to resolve internal structures. The foams, which are designed to mimic the water retention properties of porous soils, are sufficiently homogeneous to act as ideal substrates and the simulation of soil layers and void structures. Two foams, F and FF, of differing densities (*ca.*18-25 kg m^{-3}, *ca.* 27 kg m^{-3}, respectively), and shear stress were utilised. EMP profiles for uniform plain sided and stepped rods with four tip conical angles (30, 45, 60 and 90°) were

investigated. The soil proxies comprised homogeneous or alternating multilayers of FF- and F-foams. Multilayer soil stacks comprised alternating layers of 3 mm FF- and 15 mm F-foams (see Figure A1). Layers were bonded with different binding agents yielding soil structures and interfaces of various binding strengths and rigidities. Bonding methods comprised i) compression alone, provided by the light tension of external rubber bands, 'RU', ii) Uhu™ poly acrylate based glue, 'UH', iii) Pattex™ water based glue, 'PA', iv) commercial acetic silicone, 'SI', v) sugar glaze (5 parts sugar, 1 part water), 'GL'. Binding agents were distributed homogeneously on the layer surfaces resulting in *ca*. 0.5 mm thick penetrable coating. In the PA soil proxy, the bonds were denser and the glue was forming a more concentrated layer at the layer interfaces, due to glue viscosity (data not shown) being six times greater than that of UH (Figure A1). All binding agents were allowed to dry overnight.

2.4. Penetrometer measurements

2.4.1. Field Measurements:

PR of soils covered with BSCs was measured *in-situ* for 15 replicates. Five EMP measurements were made adjacent to each of the three sampling spots employed for the *ex-situ* soil samples. The distance lateral between the measurement spots was at least 10 cm to avoid interferences between the adjacent observations (Lowery and Morrison 2002). As a control the PR of unconsolidated sand at the dune crests was measured (n = 10).

2.4.2. Probe shaft geometries

The probe tip and shaft geometries employed in the EMP and idealised soil experiments are shown in Figure A2. For conical tips soil deformation occurs obliquely to the advancing conical surface of area $A = \pi H^2(sin\alpha/cos^2\alpha)$ where H is the cone height and α is the cone angle between its surface and the shaft axis (Figure A3). Plastic deformation of the soil occurs when a probe enters the surface (Figure A2a, b). This is followed by plastic yield and subsequent true shear deformation. As the dry sand soil is plastic rather than elastic, displaced soil has to flow around the probe resulting in temporary compaction in front of its leading surface accompanied by dry flow up the sides of the penetrometer shaft (Figure A2c, d). An unstepped

shaft has the same diameter as the probe tip maximal cross section, hence a frictional force exists along its length resulting in increasing resistance as the shaft advances (Figure A2d). The consequence of this on EMP profiles is discussed in more detail in the modelling section below. Where a void is encountered (Figure A2e), some spalling of the upper surface into the void is expected prior to the probe passing through the true proximal void boundary (Figure A2f). Plastic deformation is expected as the probe re-enters the soil matrix on the distal side of a void. Thus, as determined by the penetrometer pressure reading, the dimensions of voids are expected to appear slightly larger than their true physical dimension. Clearly to detect a void it must be larger than both the EMP step size and, if a conical probe is used, the cone height *H*, (see Figure A3). A discontinuity in plastic deformation stress, σ, as a function of depth, z, or $\sigma(z)$ represents a rapid transition between different soil horizons or structures. Within a BSC it is harder for material displaced by the probe to flow around the tip (Figure A2g). Thus within BSC layers increased or altered plastic (and potentially both elastic and brittle) deformation stresses are anticipated as well as altered sliding friction. Together, these factors contribute to altered soil states possessing distinctive BSC and soil depth dependent deformation stress profiles. The PR observed will also be affected by compaction, grain size and cohesion (i.e. the presence or absence of aggregates) and the presence of exotic fragments and, importantly, consistency of the shear forces applied to the penetrometer probe. Since water films at the contact points of mineral grains significantly reduce shear forces, the PR will also be greatly affected by soil moisture. Many attempts have been made to couple the measurement of PR and water content (WC) (Lapen *et al.*, 2004; Sun *et al.*, 2004; Topp *et al.*, 2003; Vaz *et al.*, 2001), despite PR being determined primarily by water tension (WT) in the soil not total volumetric water content. WT is highly variable both temporally and locally as are many other soil properties (Kuzyakov and Blagodatskaya, 2015). WT depends, for example, upon texture, structure and content of organic matter. It is generally recommended (e.g. by the American Society for Agricultural Engineers, ASAE), that if soil properties determined by penetrometers are to be compared they should possess a similar (or known) moisture content. Any PR model should attempt to take this into account, by either measuring dry soils as in this study, or by including moisture correction factors (cf. Chamizo *et al.*, 2015). For heavy duty soil

compaction penetrometers the ASAE favour conical tips with α = 30° considered to be representative of crop root tip radii and consequently used in many studies (i.e. Bengough and Mullins, 1990*;* Dexter *et al.,* 2007*;* Sun *et al.,* 2004; Vaz *et al.,* 2001). For surface or near-surface penetration resistance measurements, however, Lowery and Morrison (2002) recommend flat tipped rods. Rankine theory implies that the whilst the active zone under a conical probe corresponds closely to that of its surface a similar conical zone also exists under a flat tip (Masood and Mitchell, 1993). Whilst shear forces are dependent upon α they are smaller for a flat tip as an active conical zone of accumulated material forms below the tip. Due to the small size of our tip (D = 3 mm) the differences in shear stress between the active zone of flat and conical profile tips should, in practice, be negligible even if the soil internal friction angle were to approach 45°. For a coarse granular material, *Quezada et al.* (2014) showed that PR increases with velocity in the range $6x10^2$ to $6x10^5$ mm min^{-1}, due to the increasingly impulsive forces as the probe is pushed dynamically into the soil. This effect can be safely ignored in our measurements due to the very low velocities of only 16 mm min^{-1}. Nordal *et al.* (2013) found that the evolution of the volumetric and shear strain decreases with decreasing step size of the penetrometer. That is higher precision is achieved for small steps, as for the 39 µm step size EMP employed here. All lab and field studies have employed 3 mm diameter plain sided, flat tipped 90° probes. This has enabled maximum resolution, consistent modelling and precise investigation of BSC horizons and soil pores as discussed later in section 3.2.

2.5. Mathematical modelling of PR

Here we present a model appropriate to the description of soils covered by or incorporating BSCs. The penetration force, F, and yield stress or plastic deformation stress, σ, as a function of depth, z, of a soil or BSC are related to one another by the probe cross sectional area, A, normal to F,

$$\sigma(z) = \boldsymbol{F} \cdot \mathbf{n}/A = F(z)/A\,. \qquad (2.5.1)$$

That is $\sigma(z)$ has the dimensions of pressure, P. To drive the probe beneath the soil surface, soil must be plastically displaced below or around the probe whilst the rod experiences

frictional drag from the soil behind the advancing probe. Only if the load cell was located at the base of the tip could this frictional drag be eliminated (Anderson *et al.*, 1980), but this is only realistic for low-resolution penetrometers that work with large diameter probes. For soil containing, n, layers or (micro) horizons structurally distinct due to their differing yield stresses, we write,

$$\sigma(z) = \sigma_{c0} + \sum_1^n \left[\sigma_n(z) + \int_{z1}^{z2} F_{rn}(z)\mathrm{dz}\right] \qquad (2.5.2)$$

where σ_{c0}, and σ_n are the plastic deformation stresses for the surface and n^{th} soil structure (e.g. soil crust, layer, horizon or void) respectively. $F_{rn}(z)dz$ is the frictional work done per unit volume to slide the rod an incremental distance, dz, through the n^{th} layer. Both $\sigma_{cn}(z)$ and $F_{rn}(z)$ are related to soil structure. They determine the form of $\sigma(z)$ measured by the EMP transducer. The model enables pores (zero deformation stress) to be distinguished from changes in layer structure or probe friction. For a soil pore or void both $\sigma_n(z)$ and the frictional term $\int F_{rn}(z)dz$ are expected to be zero if the void is large enough to accommodate material displaced by the probe exiting the previous layer. If $\sigma_n(z) = 0$, $\sigma(z)$ becomes constant with depth (see Figure 2). This can occur if the tip is flat or the height of a conical tip is less than the void thickness. Only if the frictional term vanishes, e.g. at a void boundary, will $\sigma(z)$ drop discontinuously (see Figure 2). Clearly if the probe encounters an indurated surface or aggregate of grains comparable to the probe diameter, then a sudden increase in $\sigma(z)$ is to be expected. Figure 2 presents in idealised soil comprised of a series of uniform layers collectively representing buried upper and lower (fossil) crust structures interposed by a void. The structural resolution of the EMP is limited by the step size of the stepper motor (39 μm). When the sliding friction experienced by the probe is constant, $F_{rn} = a_n$, the integral in equation (2.5.2) results in linearly increasing values of $\sigma(z)$, as the probe advances to increasing depth, i.e.,

$$\sigma(z) = \sigma_{c0} + \sum_1^n [\sigma_n(z) + a_n z]. \qquad (2.5.3)$$

This assumes that sliding friction is proportional to the surface area of the shaft in contact with the soil. This frictional case is different to that of an object sliding under gravity on an inclined

plain where the frictional force is well known to be independent of surface area. Here the frictional force is proportional to the number of contact points between soil grains and the shaft sides and consequently, for a shaft of uniform diameter and a homogenous, non-structured soil, the frictional force increases linearly with insertion depth. The lateral force pressing the grains against the shaft is mainly due to deformation rather than hydrostatic pressure as a dry soil column is largely self-supporting. Fluctuations in sliding friction are proportional to the number of contact points and the area over which they act by $\delta F \propto (nA)^{-1/2}$ (Persson, 2000). Importantly, equation (2.5.3) demonstrates that if sliding friction is experienced by the whole probe, then even for structurally uniform soil, the *apparent* value of $\sigma(z)$ determined via the penetrometer force transducer will increase monotonically as the probe is driven to ever increasing depths. If sliding friction changes linearly with depth, (due, for example, to increasing compaction, decreasing porosity or increasing gravimetric pressure) and may be described by a first order polynomial, $F_{rn} = a_n + b_n z$, then a square law will be observed for the frictional component, i.e.,

$$\sigma(z) = \sigma_{c0} + \sum_1^n [\sigma_n(z) + a_n z + b_n z^2]. \qquad (2.5.4)$$

This has been observed in unconsolidated sand, (see Figure A5). Consequently, if subcrust structures are to be correctly identified or characterised from $\sigma(z)$, it is necessary to distinguish between structural effects that determine the force needed to advance the penetrometer probe and those due to frictional forces acting on the penetrometer. Equation (2.5.2) also permits the deformation stress of specific layers (such as one containing a fossil BSC) to be modelled using a distribution of shear stresses. That is, the shear stress varies continuously throughout the crust. Here we have used the lognormal function to model asymmetric crust deformation stress. Due to the changing structure and biotic components of BSCs, they are not generally expected to be structurally symmetric about their centre plane. Clearly a number of factors may cause changes in the deformation stress with depth even in a mineralogical uniform soil (as is the case in the NW Negev). In which case equation (2.5.2) accommodates any appropriate functional description of $\sigma_n(z)$ although we find a simple second order polynomial

description is often sufficient. Here we use one similar to that employed for the frictional term, namely,

$$\sigma_n(z) = \alpha_n z + \beta_n z^2. \qquad (2.5.5)$$

Experimentally, we seek to detect and quantify BSCs and related structures within the soil. That is, uniform values of $\sigma(z)$ are of less interest, providing only background information. In contrast the spatial differential, $P' = d\sigma_n/dz$, detects only change and enhances layer detection. From equation (2.5.2) it is seen that,

$$P' = \sum_1^n \left[\frac{d}{dz}\sigma_n(z) + F_{rn}(z) \right]. \qquad (2.5.6)$$

Thus a BSC layer should manifest itself as a peak or inflection in P' and a homogeneous background soil structure as a horizontal or low gradient region. Consequently a soil column containing only horizons of uniformly structured soils is expected to exhibit a series of horizontal or low gradient structures. If $\sigma_n(z)$ is constant in each layer, P', equation (2.5.6), reduces to the sum of F_{rn} alone. Hence we use spatial differentials, P', to interpret PR field data. In practice we typically employ five, seven or nine point sliding window averages to the raw experimental data to minimise high frequency noise artefacts and structural noise to make the effect of genuine soil structures upon P and P' clearer.

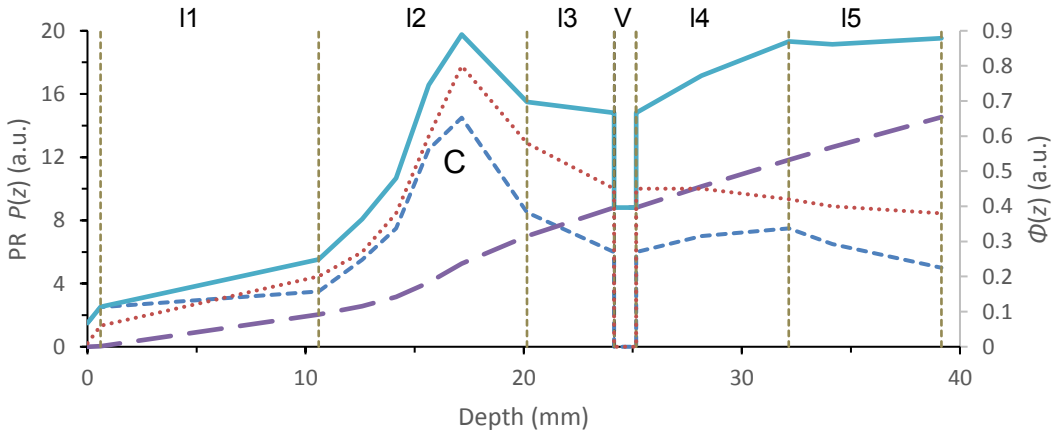

Figure 2: An idealised soil comprising five layers (I = 1, 2, 3, 4, 5), a buried crust, C, and a void (V). Each primary layer (bounded by vertical dashed lines) has a distinct shear stress, σ_n, (short dashed line) and characteristic frictional drag (F_n, dotted line). Total frictional drag increases

with depth ($\Phi = \int F_n \, dz$, long dashed line). Drag and shear stress combine to produce EMP soil profile (*P*(*z*), solid line). See model for further explanation.

2.6. Penetrometer behaviour in idealised soils

Probe tip geometries: As the applied force, F, is normal to the cross sectional area of the probe, the maximum force required to penetrate a soil is independent of the probe surface area whatever its shape once fully immersed in the soil. For a flat tip (α = 90°) F is normal to the probe axis over area $A_\perp = \pi D^2/4$. For partial penetration of a conical tip, i.e. z < H, the apparent shear stress is,

$$\sigma_z = \sigma_0 \, A_\perp(\alpha, z)/(\pi D^2/4) \qquad \text{where} \qquad A_\perp = \pi z^2 tan^2\alpha \qquad (3.1.1)$$

The EMP records a surface deformation force increasing nonlinearly as z^2 prior to full penetration at depth $z = H$ where $H = D/(2tan\alpha)$. In this study for D = 3 mm and α = 30, 45, 60 and 90°, the corresponding values of H are 2.60, 1.50, 0.87 and 0 mm. Once fully inserted into the soil conical tips average fluctuations in the shear stress over H. Conical tips also encourage purging of the displaced soil away from the cone apex. For stepped shafts the un-stepped length, l, below the conical tip was 1 mm (Figure A3). Prior to full engagement of the probe into the soil P is an underestimate of the shear stress unless the insertion force is normalised to the cone surface area engaged with the soil (Figure A4a). The true shear stress is only measured once the tip is fully immersed, (Figure A4b).This difference can be significant when attempting to study small scale changes in the surface soil and surface crust strength unless a flat tipped probe (α = 90°) is employed. Only for flat tips does the idealised penetration profile and hence penetration shear stress occur at the surface. Figure 3 and Figure 4 show the EMP deformation stress for foams F and FF, the latter *ca.* 3x firmer than the former (Table A1). Solid lines represent model equations, dashed lines experimental data (n = 5). Almost identical dependence with probe geometry is seen for both foams except that the increased rigidity of FF yields more reproducible curves. Figures 3a, b and 4a, b demonstrate the effects of cone angle upon apparent initial shear stress as the cone becomes fully immersed in the

foam as discussed above. The incremental precision of the EMP makes it possible to observe surface plastic and / or elastic deformation as the probe enters the foam, that is, the experimental data typically lag the model curves by 0.5 mm. Once the probe is fully immersed both plain and stepped shafts behave in a similar manner, $P(z)$ increasing linearly to z ~ 5 mm. The initial (linear) frictional terms, a_n, are similar for all tip profiles (Figures 3a,b and 4a,b) although they differ between shaft geometry (Table 1). For z > 5 mm $P(z)$ depends upon probe angle, (Figures 3c, d and 4c, d). For both foams and stepped shafts, the behaviour of α = 90° (flat) and α = 60° tips are similar, a_n, ~2.3 kPa mm^{-1} to z ~ 10 mm (Figures 3c, 4c). Thereafter, the frictional term becomes close to zero as the curves flatten especially for the stiffer foam, FF. The flat curve for 30° tips indicates a very low and constant frictional term albeit at the cost of vertical acuity. With the exception of the 90° plain shafted probe, frictional terms are lower for stepped rods (Table A1 and Figures 3, 4). Stepped rods with 30° and 45° tips have the lowest and almost identical low frictional behaviour. For a given shaft geometry the curves for 30° and 45° and 60° and 90° probes tend to overlie one another. Stepped sided shafts with α > 45° give almost depth independent shear stress curves. We interpret the plateau like curves for stepped tips as indicative of flow into the accommodation volume that forms behind the advancing probe. With the exception of the plain shaft 60° probe, which has the lowest frictional term F_{rn} for both foams, F_{rn} increases with α for plain shafts. Fluctuations in $P(z)$ are observed, on a length scale which suggesting that they are due to structural variations in the foam. For α = 30° and 45° the F_{rn} becomes close to zero for z > 10 mm (Table 1). In summary, we find that cone angle affects the vertical resolution but, in general, makes little difference to the frictional term which is lowest for stepped sided shafts. Whilst the lower frictional loading of stepped rods offers some advantages, especially in wet soils where friction is largely dependent on WT, they leave the soil column unsupported after passage of the probe through the soil, which is of importance in sandy soils with a low intrinsic aggregate stability. Although plain sided shafts (Figures 3d, 4d) display larger sliding friction it is reproducible with depth. Further, our model permits the effects of sliding friction and plastic deformation to be distinguished. Thus plain sided shafts offer the possibility of consistent modelling and

interpretation of field measurements of $P(z)$ at the small cost of a larger frictional term. For these reasons, as reported in section 2.4.2 all lab and field studies employed 3 mm plain sided, flat tipped probes to enable maximum resolution and consistent modelling and precise investigation of BSC horizons and soil pores.

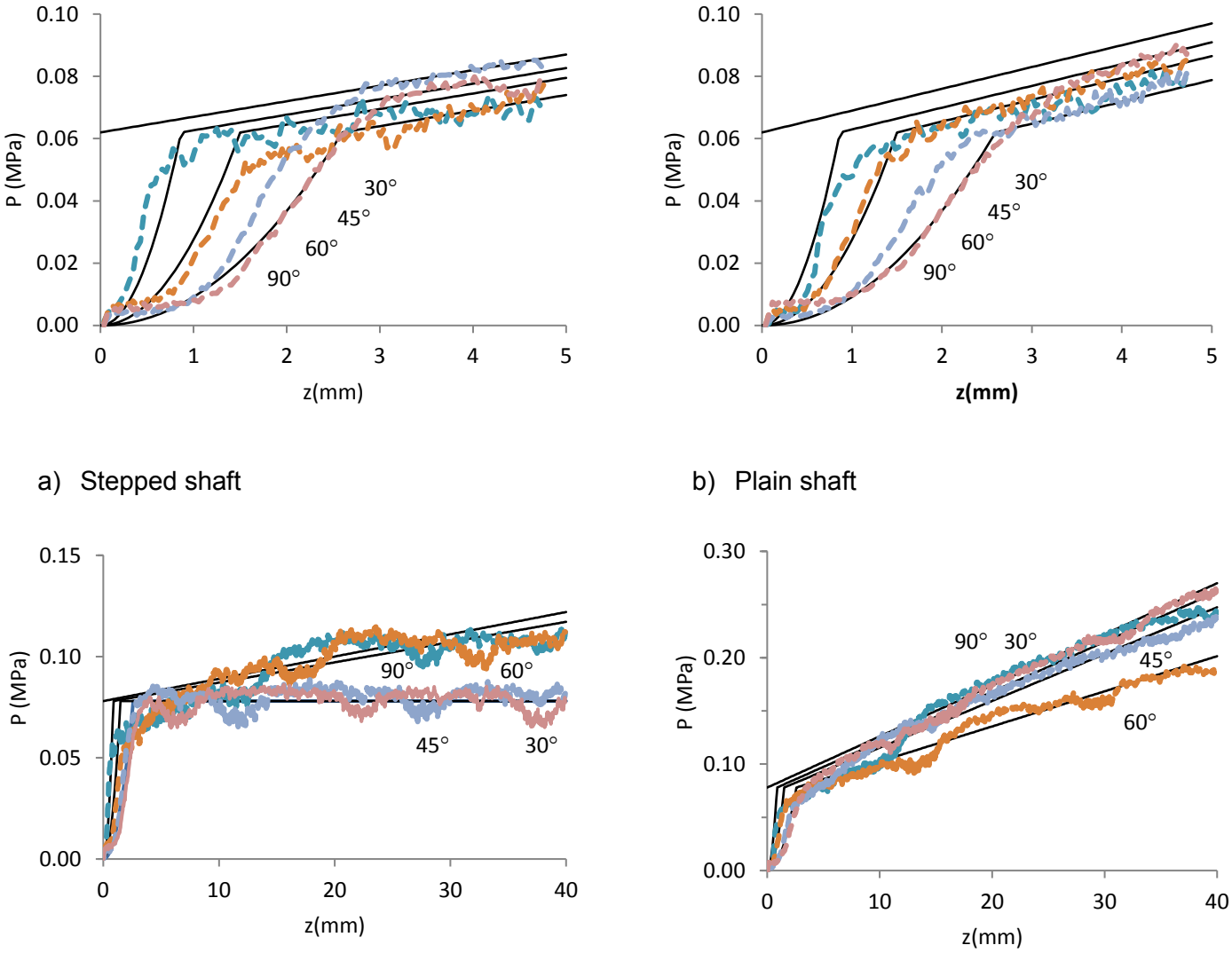

a) Stepped shaft

b) Plain shaft

c) Stepped shaft

d) Plain shaft

Figure 3: Initial and full probe penetration depth EMP curves for ideal soil material F using 90°, 60°, 45° and 30° tips on stepped (a, c) and plain sided (b, d) shafts, respectively; solid lines model equations, dashed lines experimental mean data (n = 5).

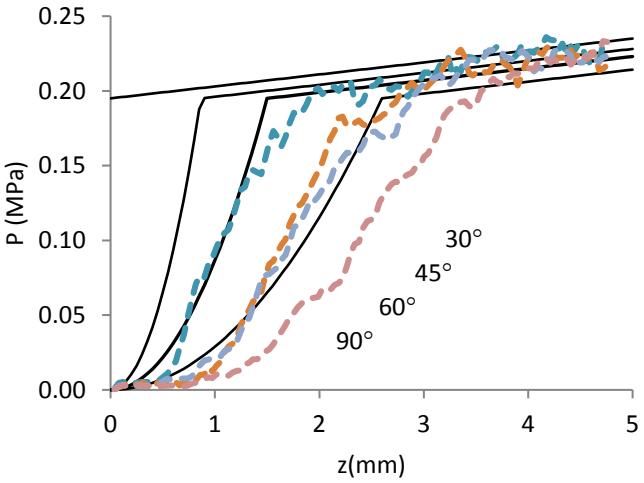

a) Stepped shaft

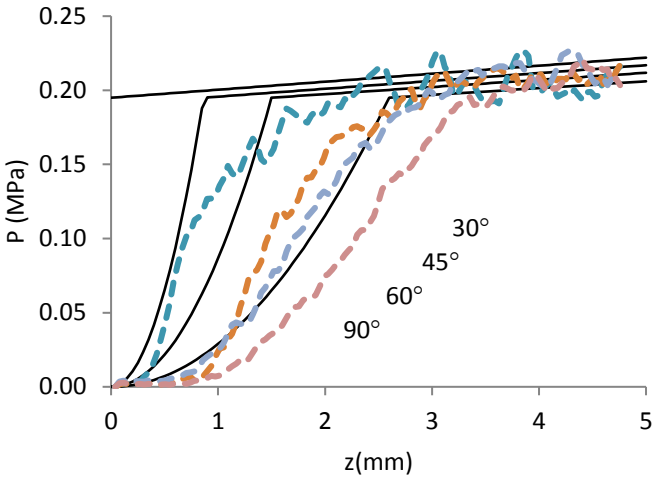

b) Plain shaft

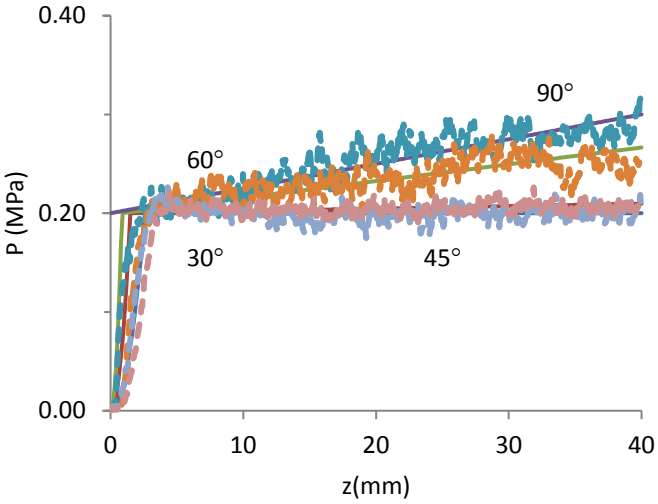

c) Stepped shaft

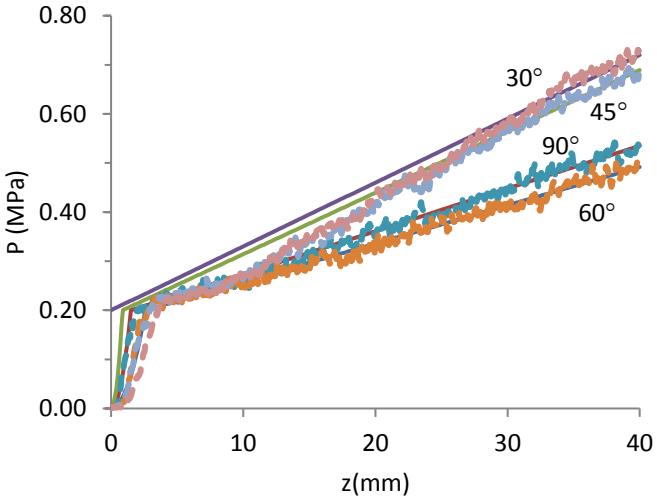

d) Plain shaft

Figure 4: Initial and full probe penetration depth EMP curves for ideal soil material FF using 90°, 60°, 45° and 30° tips on stepped (a, c) and plain sided (b, d) shafts, respectively. Solid lines (in a and b) represent the model equations, dashed lines the experimental mean data (n = 5).

2.7. Artificial layering in idealised soil proxies

The effect of the five different binding agents (see section 2.3) upon $P(z)$ and $P'(z)$ is seen clearly in Figure 5 and Figure 6, respectively. In RU, no chemical bond was used, only light external compression analogous to hydrostatic pressure. Thus the layers are materially unaltered and the structures observed in the penetrogram and its (sharper) spatial differential are purely the result of the probe traversing the differing layers F and FF. The UH penetrogram is similar to that of RU although broader near interface regions indicating that the UH bond is relatively weak and extended consistent with dilution of the binder during preparation. The same is true of $P'(z)$ for UH. Here, none of the small sharp negative peaks visible in RU are seen consistent with less deformation of the foam regions bonded by interfacial glue. In comparison with the F/UH/FF soil proxy, the interface bonds of the F/PA/FF soil proxy were denser consistent with the adhesive having formed a more concentrated and rigid interface layer (Figure A1) evidenced by the behaviour of $P(z)$ and $P'(z)$. In homogeneous regions spatial differentials exhibit zero or low gradients as expected (section 2.5) due to the absence of structural heterogeneities. Although PA has the greatest rigidity and shows the highest values for PR_{max}, it does not exhibit a steep decline in $P(z)$ at either side of the interfaces as is observed for the RU, UH and GL soil proxies. This is indicative of a strong and continuing drag upon the penetrometer shaft after it has broken through the PA bond at an interface. Binding agent GL formed the most rigid bond consistent with the steep fall of $P'(z)$ at *ca*. 3.4 mm (Figure 5) after penetration of the initial layer. The most negative $P'(z)$ value observed occurs at 4.1 mm for binding agent GL and is larger in magnitude than the corresponding positive value (Figure 6b) indicative of bond asymmetry or residual drag on the shaft. PR before the break is not as steep consistent with weak dragging on the penetrometer shaft by the sugar based interface bonding agent. In contrast, the silicone bonded (SI) soil proxy does not exhibit an unequivocal break point in the $P(z)$ profile. Rather, a broader more rounded shape to the curve and a comparatively high PR_{max} and fairly low values of $P'(z)$ are observed as might be expected for a strong but elastic bond. The absence of any strikingly steep positive or negative $P'(z)$ peaks is also consistent with a flexible bond. Figure A6 shows the behaviour and model fit to the penetrometer probe passing perpendicularly through two approximately cylindrical

voids in a homogeneous model soil. The layer model has been computed as a series of layers of common material constrained to approximately identical shear stresses and frictional terms. The exit regions from the two voids are not modelled here but represent an apparently declining shear stress as the probe exits the unsupported void wall approximately mirroring the entry region. Overall, the behaviour of $P(z)$ and $P'(z)$ for the soil proxies and different cone angles for the narrow (3 mm) diameter tips is generally consistent with a small conical active zone under the plain tips similar to that predicted for conical ones.

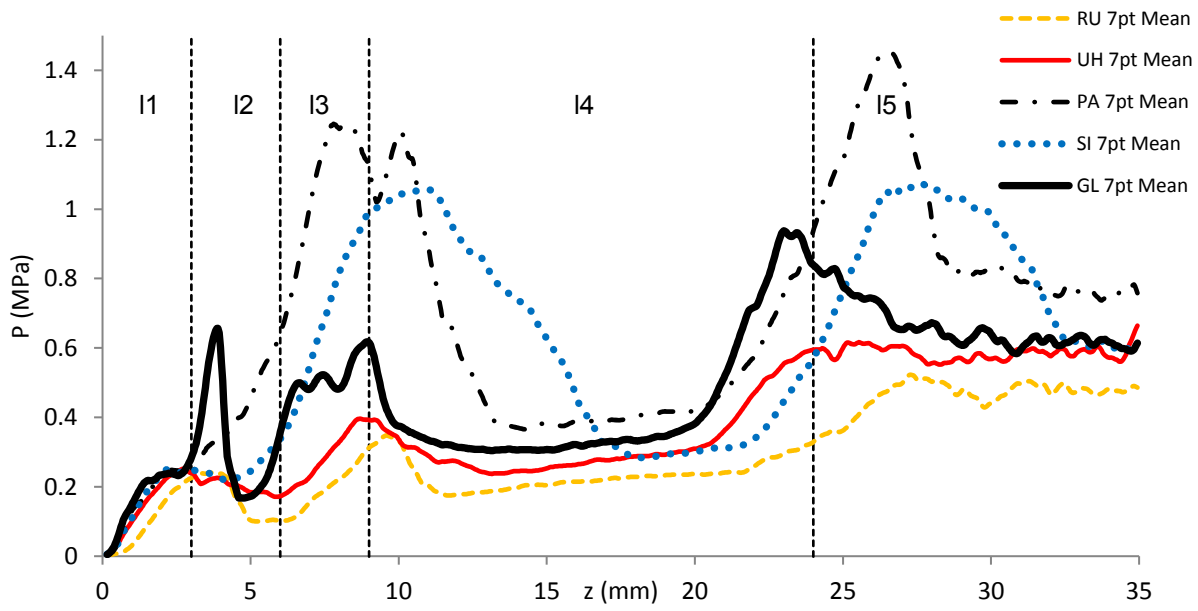

Figure 5: $P(z)$, n = 5, for bonding agents, RU, UH, PA, SI, GL, in 5 layer (l = 1, 2, 3, 4, 5) proxy soils. Vertical dashed lines indicate layer boundaries.

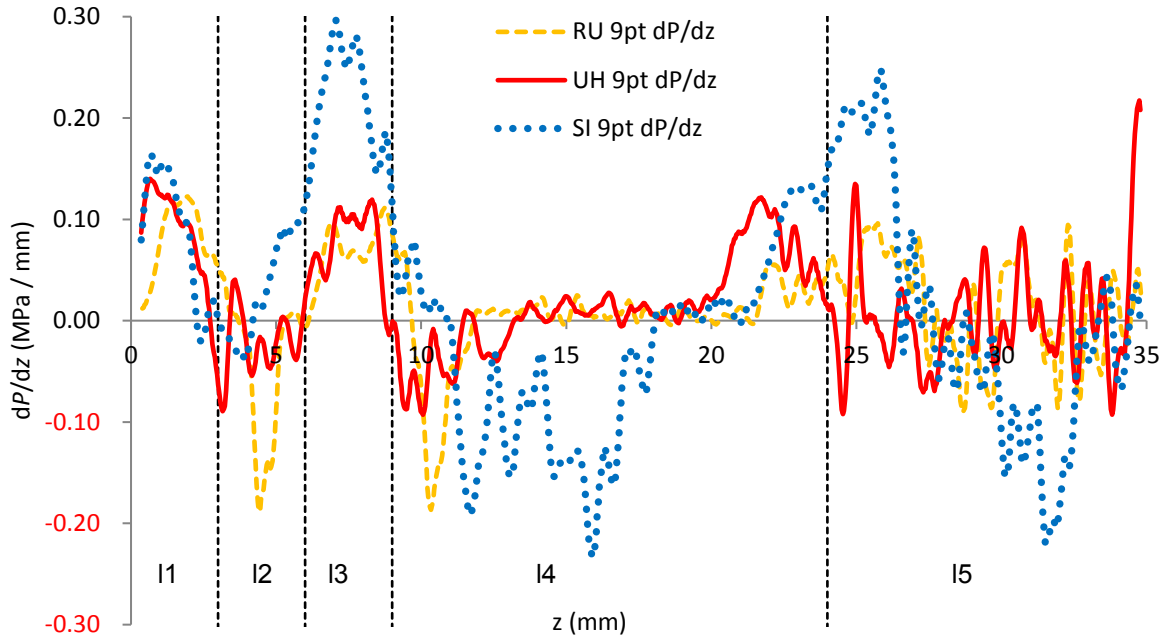

a)

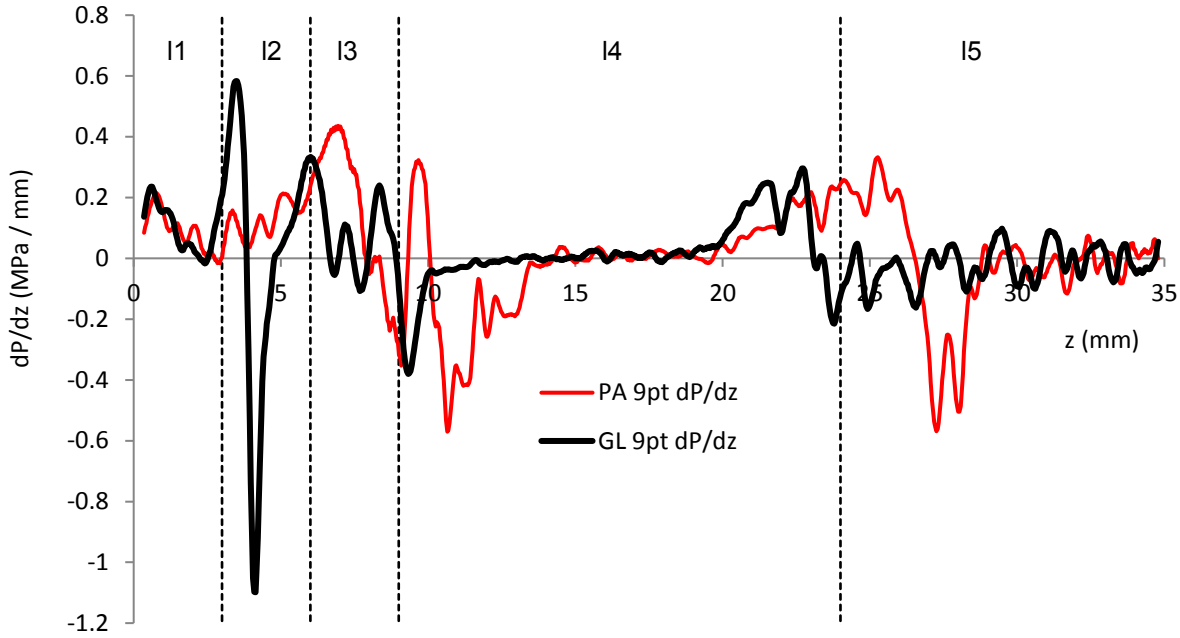

b)

Figure 6: Spatial differential, P'(z), n = 5, for bonding agents (a) RU, UH, SI and (b) PA, GL in 5 layer (I = 1, 2, 3, 4, 5) proxy soils. Vertical dashed lines indicate layer boundaries. Homogeneous regions have zero or low gradients.

3. Results

3.1. Contextual field observations

The loose sand that covered the crust in Figure 7a in the Nizzana-south site was blown off to expose the buried crust. The burial depth ranged from 5-10 mm. Figure 7b was taken farther away from the mobile dune crest, where oversanding occurs less frequently. Here the young cyanobacterial crust had time to regrow on top of an older fossilised crust visible at a depth of about 15-20 mm.

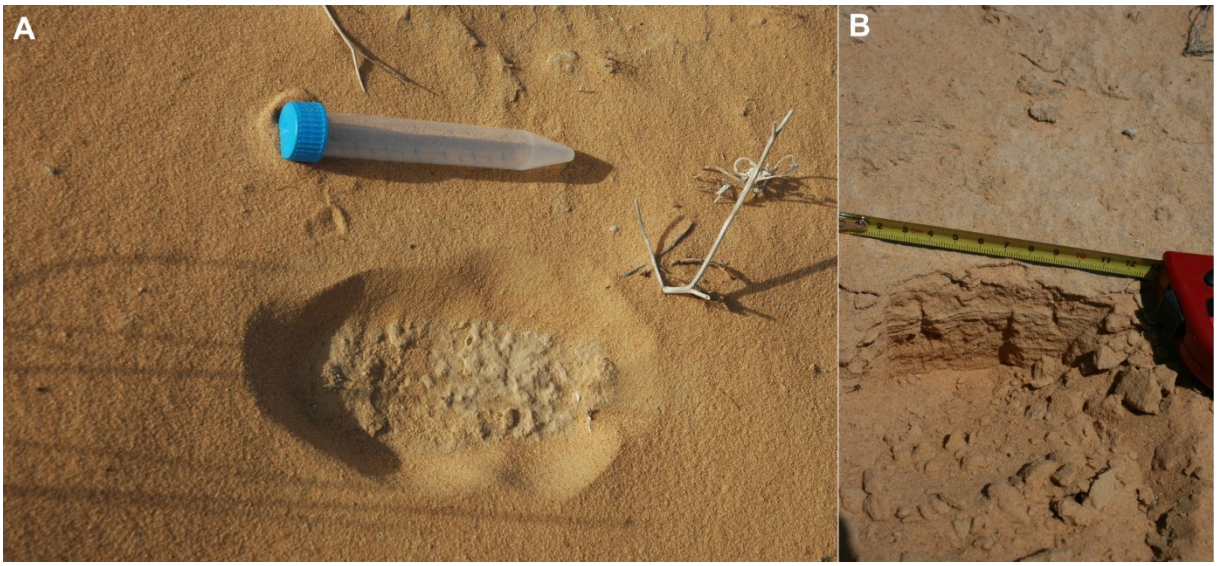

Figure 7: a) Severely oversanded cyanobacterial soil crust on the south facing slope of a sand dune in Nizzana-south on April 22nd, 2012. b) Photo of a buried crust at about 2 cm depth with a younger and thinner new crust developing on top, taken on March 29th, 2011.

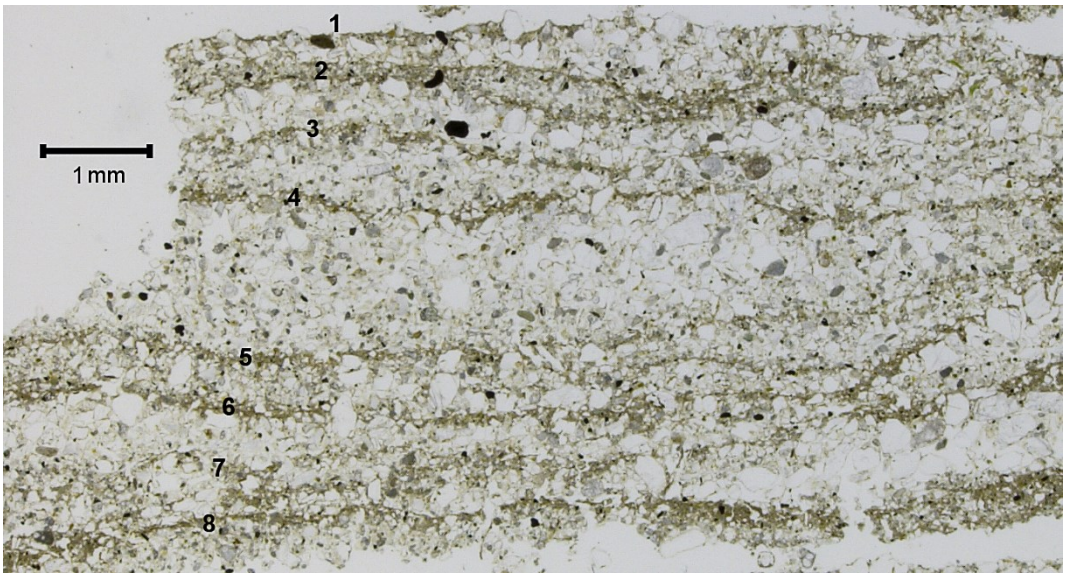

[a]

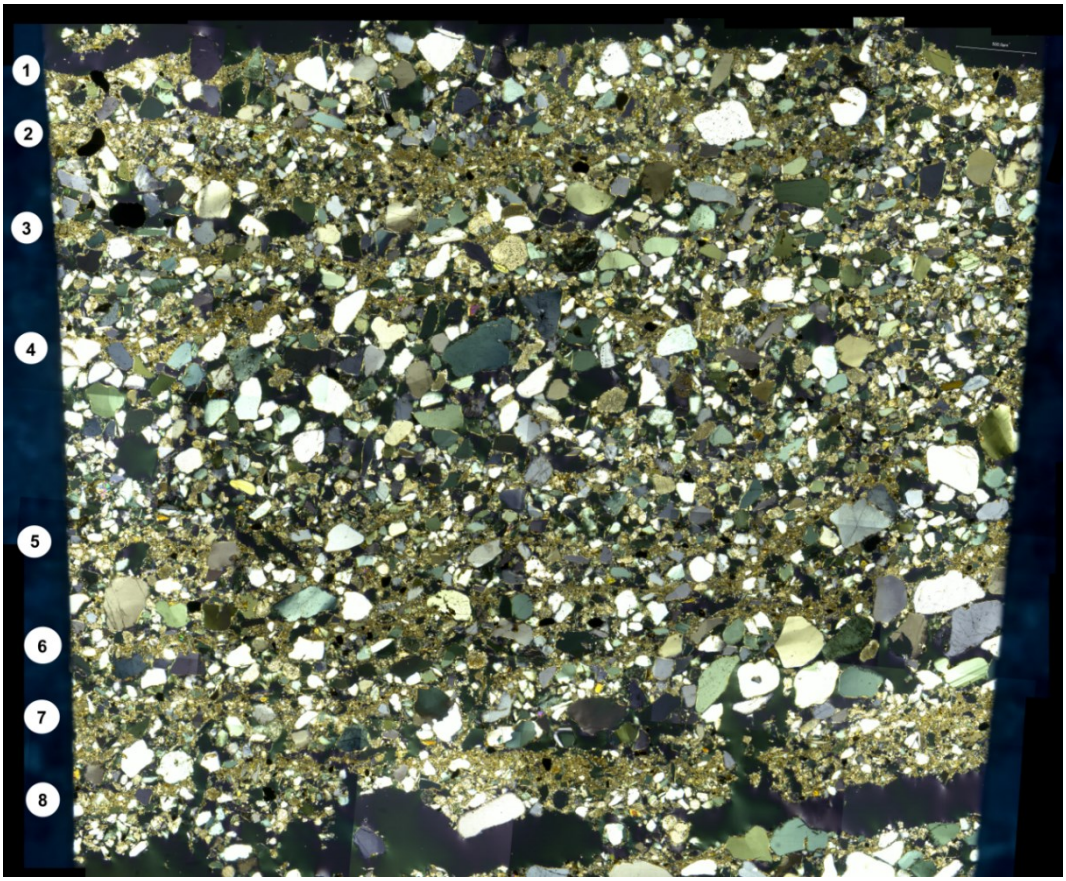

[b]

Figure 8: [a] Microscopic thin section, showing at least eight layers of fines, i. e. oversanding / recolonization surfaces. [b] The thin section under cross-polarized light, distinguishing between (bright) mineral grains and (black) pore space. Numbers indicate equivalent zones in [a] and [b].

3.2. Ex-situ optical measurements

The numbers, 1 to 8, in the microscope thin sections of Figure 8a & b denote equivalent buried fines associated with BSC zones indicating frequent oversanding and recolonization of a new oversanded surface. Cross-polarised light microscopy (Figure 8b) allows clear distinction to be made between mineral grains (bright contrast) and pore space (black contrast). The larger pores (dark contrast) are typically associated with regions in which coarser grains occur. These are more likely to be displaced while the EMP-probe is advancing. Similarly, large grains will tend to increase the vertical dimension of the active conical zone below the probe tip resulting in increased frictional losses and apparent shear strength.

3.3. Modelling of field data

All figures in this section show the force $P(z)$ or $P'(z)$ required to advance the probe step-wise in 39 μm increments through oversanded buried BSC sand soils. A sliding window average and base line fitting assists in distinguishing the contribution of the BSC from the sand substrate. $P(z)$ in Figure A5 represents an average over 10 profiles for a bare loose sand soil fitted with a second order equation (eqn. 2.5.4) for $z < 17$ mm. This is effectively a baseline, which if compared to crusted soils, gives a measure of the effect of BSCs upon the soil strength. A similar second order dependence is observed for the deeper sand (fit not shown for clarity). The differences between un-compacted loose sand and soil profiles containing buried BSCs is striking (see below) and so in practice, we have found it unnecessary to subtract externally determined baselines from field profiles when using the penetrometer model. This is advantageous, as to do so could introduce unknown artefacts.

3.4. Modelling of the buried crust data from Nizzana-south

Figures 9 to 13 show *in situ* EMP soil profiles from the Nizzana-south field site, identified as profiles S156, S158, S159, S160, S162. These profiles are representative of those observed along transects using the soil penetrometer. Here we extend the penetrometer model to include the contribution from multiple buried crusts. This has resulted in data fits which unequivocally support ex-situ optical microscope and in-situ structural field observations in soil pits (cf.

Figures 7, 8 and Figure A7), namely that the study site is subjected to frequent oversanding crust burial events. The subcrust (uncrusted) soil baseline parameters were initially constrained by modelling profile S156 (Fig. 9a), the profile with the simplest structure, using a model incorporating four intrinsic soil shear stress regions and frictional terms alone. This baseline model was then applied to all other profiles (S158, S159, S160, S162). The vertical dotted lines represent the model depths at which the baseline soil strength changes (four regions in total), whilst the dashed line indicates the common (or very similar) soil baseline. It is apparent from Figures 9 to 13 that in addition to these regions up to four buried crusts are present. The fits to the experimental data were then refined by adding up to three 'fossil' buried crusts. The log-normal distribution function (LNDF), characterised by two parameters μ and σ, was found to fit single surface BSC profiles with high accuracy. The LNDF has been utilised for all buried crusts enabling the BSC $P(z)$ asymmetry about the crust centroid to be modelled accurately and simply. The BSC peak occurs at the LNDF median depth, which is taken as the modelled crust position. At large values of (standard) deviation parameter ($\sigma > 0.2$) the LNDF peak position moves to increasingly greater depths and the distribution broadens and flattens. Figures 9 to 13 show the model components (baseline dashed, and BSC LNDF components solid lines). The summative multi-component model fit underlies the experimental data. Extremely good agreement between the model and the experimental profiles is seen for all profiles. Buried fossil crusts, C1, C2 etc., occur at similar depths with one weaker remnant observed in four profiles at 25 to 30 mm depth. They are all described by similar modelling parameters giving credence to the notion that they have been formed under similar eco-environmental conditions. In some of the EMP profiles there are regions that could be construed as either a change in soil structure or weak remnant BSC crusts. The latter option has been chosen in general but never required more than four buried crusts to be postulated. In Figures 9 to 13 the full model curve is of sufficient accuracy to underlie the (noisier) experimental data almost without exception across the whole experimental depth range of 40 mm. Figure 9a, profile S156, exhibits a strong (3.1 MPa) thin surface crust at 2.5 mm, plus one strong and one deeper weaker buried crust at 13 and 26 mm respectively, two fossil crusts in

all. Figure 9b) shows the spatial differential (after a 5-point smoothing average applied) indicating the strong surface crust and relative homogeneous nature of the deeper soil perturbed by the buried crusts. Figure 10, profile S158, exhibits a strong surface crust (2.1 MPa) at 1.5 mm underlain by an even stronger (2.9 MPa), possibly more recently buried subcrust at 2.5 mm and three deeper fossil crusts, at 6, 9 and 20 mm respectively, four fossil crusts in all. Figure 11a, profile S159, shows a strong surface crust at 1.5 mm beneath which is another at 5 mm and possibly a more weakly resolved crust at 3 mm, which is also indicated by the spatial differential in Figure 11b. Two deeper crusts exist at 9 and 25 mm, i.e. four buried crusts in total. Figure 12, profile S160, exhibits a weaker surface crust and three shallow weak fossil crusts between 3 and 8 mm, plus one strong deep crust at 24 mm. Compared to the previous three plots, for S160, the baseline plot (dashed line) has been optimised in the deepest model layer to increase slightly with depth ($z > 6$ mm). For S160 the weakest buried crust implied by the model is only of 0.14 MPa strength. Figure 13, profile S162 exhibits one moderate strength surface crust and a strong fossil (3 MPa) crust at 14 mm. Also, three additional weaker fossil crusts appear above and below the stronger buried crust.

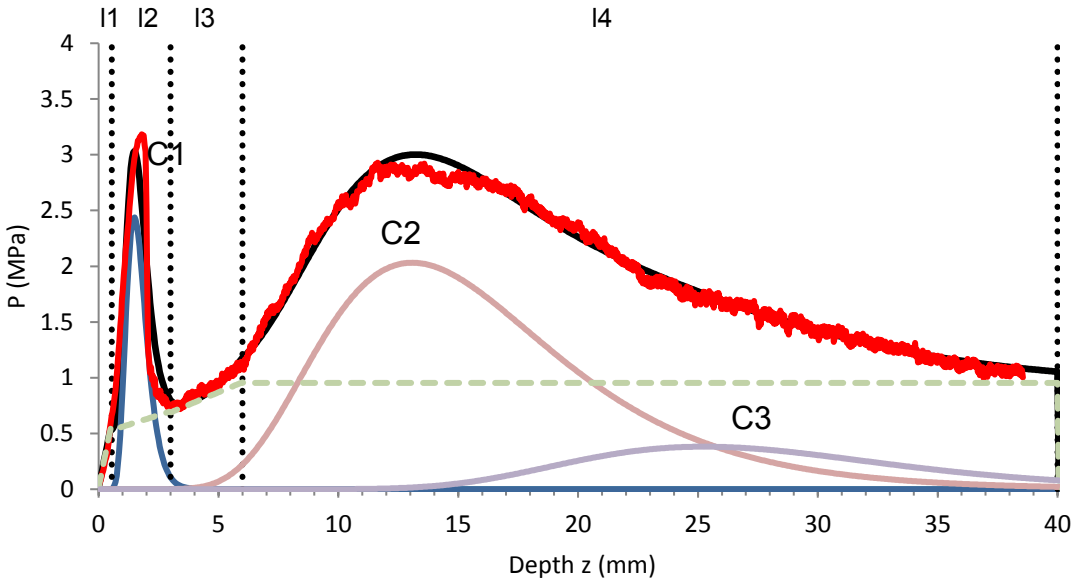

a)

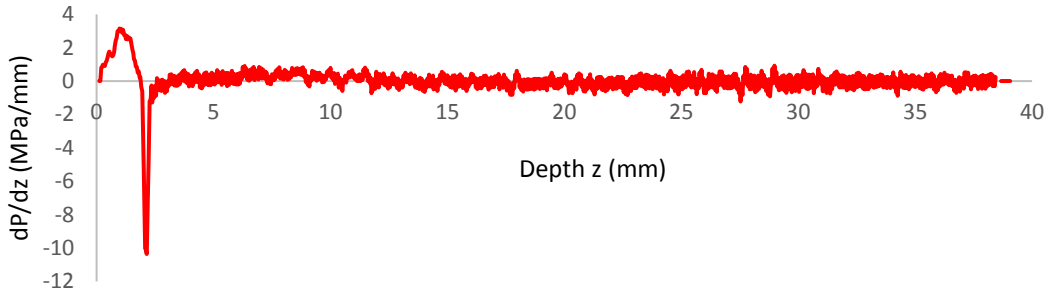

b)

Figure 9: a) S156 'noisey' experimental data and 'smooth' heavy black line model fit. The model shows a surface crust at 1.5 mm and two buried crusts at 13.1 and 25.2 mm resp. b) *P'* indicating the strong surface crust and deeper soil perturbed by the buried crusts

Descriptive Key (common to Figures 9 to 13 inclusive): Vertical dotted lines indicate distinct uncrusted soil regions. Buried crust components, C1, C2 etc., detected by the model shown by smooth peaks rising from the baseline. The light grey dashed lines indicate the soil frictional baseline, common to this and following figures.

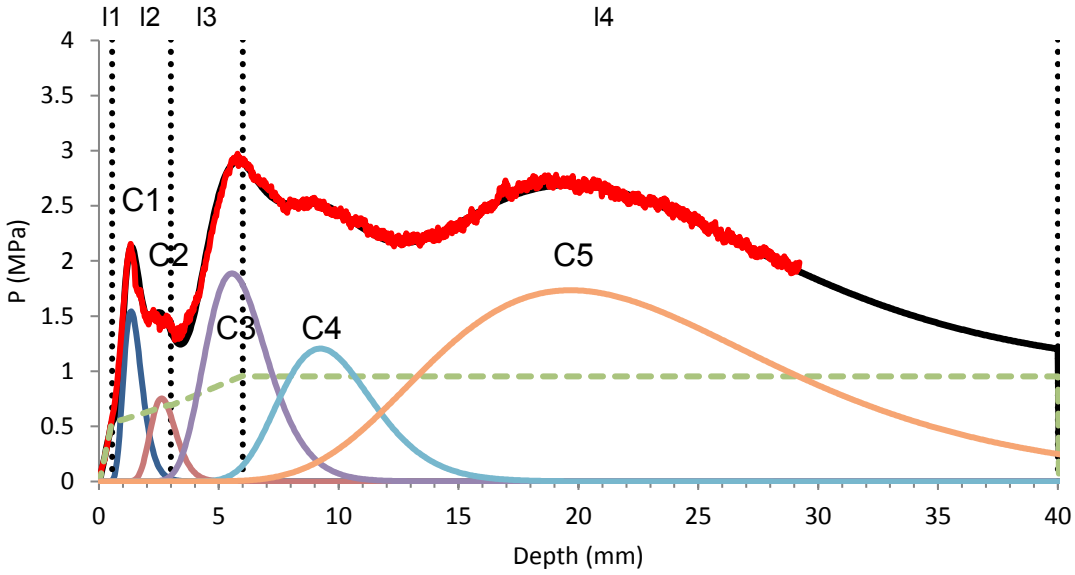

Figure 10: S158 – exhibits a strong surface crust (at 1.3 mm) underlain by a more recently buried subcrust (at 2.6 mm) and three deeper fossil crusts, (i.e. 5.5, 9.2, and 19.7 mm resp.), five crusts in all.

The primary fitting parameters used to model the surface and buried soil crusts in figures 9 to 13 are given in Table 1. Surface crust contribute between 60 % and 80 % of the surface soil strength. From the peak shear strengths of the buried crusts it can be seen that they contribute anywhere between 10 % and 80 % of the soil strength at a given depth demonstrating the importance of fossil BSCs to soil strength and thus (ultimately) landscape stability.

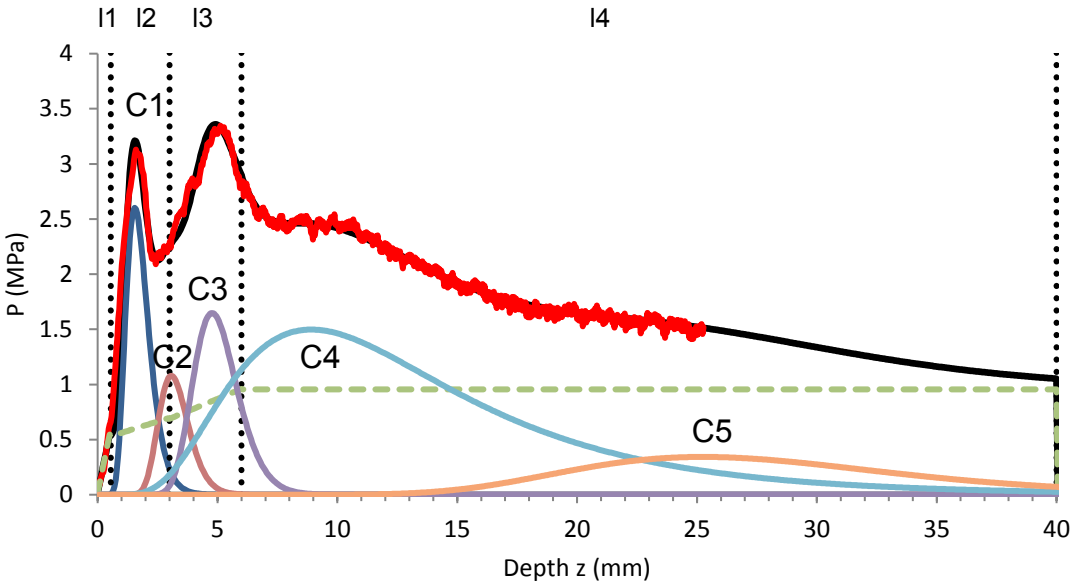

a)

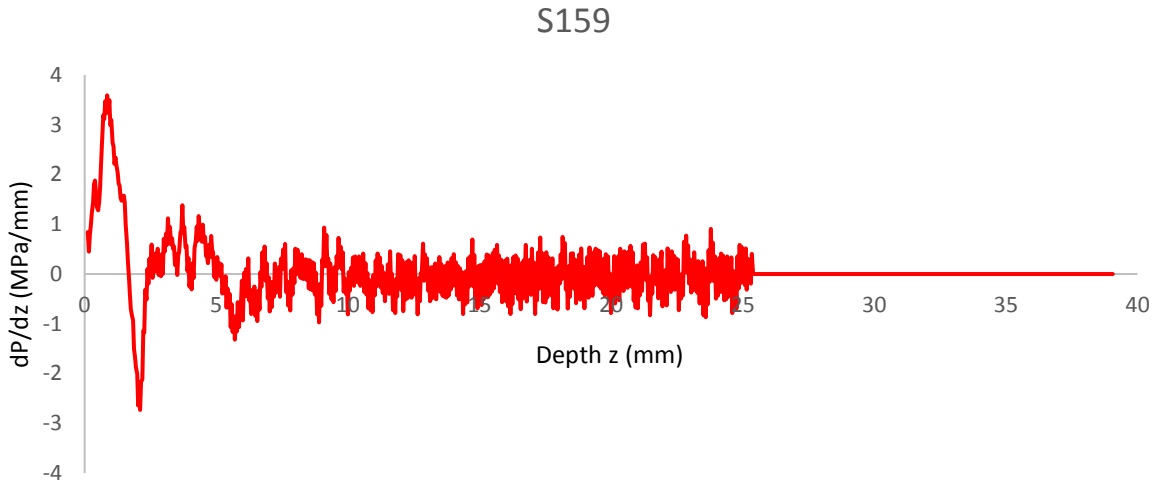

b)

Figure 11: a) Profile S159, one surface crust (1.6 mm) and 4 buried crusts (at 3.1, 4.8, 8.9 and 25.2 mm resp.) b) d*P*/d*z* (5-point smoothing average applied) indicating the strong surface crust and a second buried crust (at 5 mm) with two weaker regions directly below the crust peaks (2 mm and 5.5 mm, respectively).

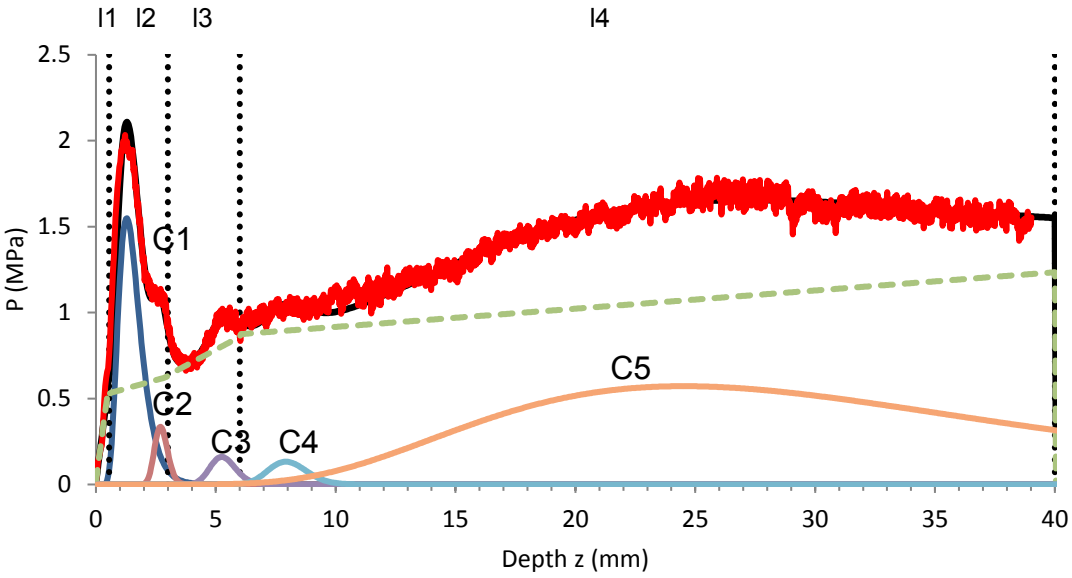

Figure 12: Profile S160, one surface crust (at 1.3 mm), three shallow weak fossil crusts between ~3 and 8 mm (i.e. 2.7, 5.2, 7.9 mm) and one strong deep crust at 24.5 mm. Baseline plot (dashed line) adjusted to increase slightly with depth.

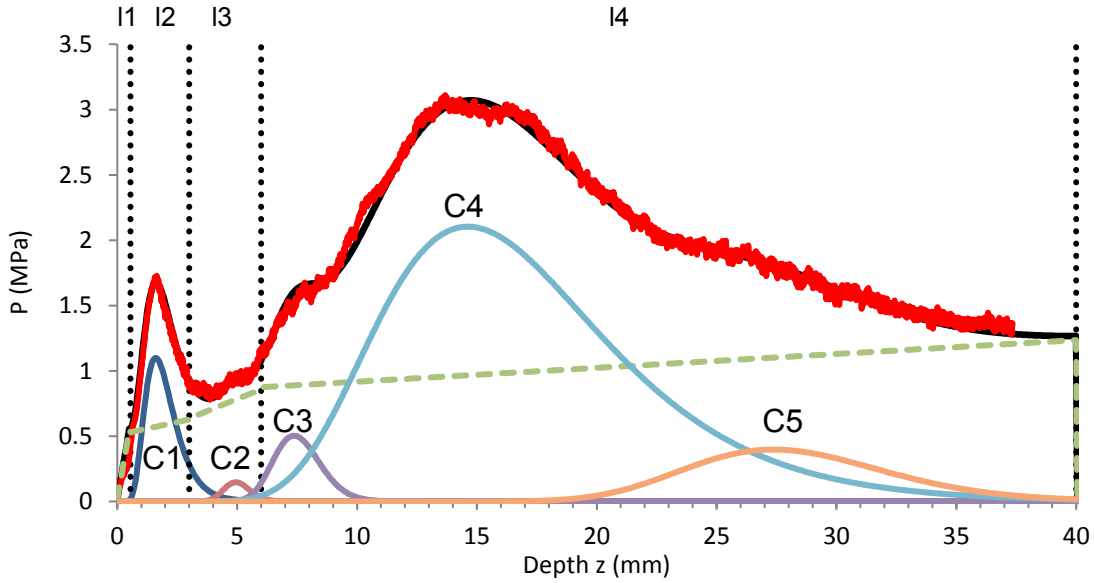

Figure 13: Profile S162 one surface crust (at 1.6 mm), a strong fossil crust, at 14.6 mm, and three additional weak fossil crusts (at 4.9, 7.4 and 27.4 mm respectively), i.e. 4 buried crusts in total.

Table 1: The primary fitting parameters used to model the surface and buried soil crusts in figures 16 to 20

	Model Parameters	Top Crust	Buried 1	Buried 2	Buried 3	Buried 4
S156	Modal (Peak) Crust Depth (mm)	1.5	13.1	25.2		
	Crust Strength (MPa)	2.44	2.03	0.38		
	Total Strength (MPa)	3.02	3.00	1.76		
	Residual Soil (MPa)	0.59	0.95	0.95		
	Crust / Local Soil Strength (%)	**81**	**68**	**22**		
	LNDF μ	1.61	15.00	27.00		
	LNDF σ	0.28	0.37	0.26		
S158	Modal (Peak) Crust Depth (mm)	1.3	2.6	5.5	9.2	19.7
	Crust Strength (MPa)	1.54	0.75	1.89	1.20	1.73
	Total Strength (MPa)	2.12	1.53	2.86	2.51	2.08
	Residual Soil (MPa)	0.58	0.67	0.92	0.95	0.58
	Crust / Local Soil Strength (%)	**73**	**49**	**66**	**48**	**84**
	LNDF μ	1.45	2.72	5.85	9.65	22.40
	LNDF σ	0.28	0.20	0.23	0.21	0.36
S159	Modal (Peak) Crust Depth (mm)	1.6	3.1	4.8	8.9	25.2
	Crust Strength (MPa)	2.60	1.08	1.65	1.50	0.34
	Total Strength (MPa)	3.21	2.27	3.34	2.46	3.21
	Residual Soil (MPa)	0.60	0.69	0.85	0.95	0.60
	Crust / Local Soil Strength (%)	**81**	**47**	**49**	**61**	**11**
	LNDF μ	1.70	3.20	4.95	11.80	27.00
	LNDF σ	0.30	0.20	0.19	0.53	0.26
S160	Modal (Peak) Crust Depth (mm)	1.3	2.7	5.2	7.9	24.5
	Crust Strength (MPa)	1.55	0.33	0.16	0.13	0.57
	Total Strength (MPa)	2.10	1.12	0.96	1.05	2.03
	Residual Soil (MPa)	0.56	0.61	0.80	0.90	0.56
	Crust / Local Soil Strength (%)	**74**	**30**	**17**	**13**	**28**
	LNDF μ	1.45	2.72	5.30	8.00	30.00
	LNDF σ	0.35	0.10	0.10	0.10	0.45
S162	Modal (Peak) Crust Depth (mm)	1.6	4.9	7.4	14.6	27.4
	Crust Strength (MPa)	1.10	0.15	0.50	2.10	0.40
	Total Strength (MPa)	1.67	0.95	1.60	3.07	1.63
	Residual Soil (MPa)	0.57	0.78	0.89	0.96	0.58
	Crust / Local Soil Strength (%)	**66**	**16**	**31**	**69**	**24**
	LNDF μ	1.85	5.00	7.50	16.20	28.00
	LNDF σ	0.38	0.11	0.13	0.32	0.15

4. Discussion

4.1. Implications of crust layering for soil properties and functions

4.1.1. Soil behaviour

Soils are generally considered to be an elastoplastic medium depending on texture and matrix potential. The BSC / sandsoil systems studied here tend towards incompressibility and are comparatively rigid and inelastic, similar to the artificial soil proxies. The “concentration factor” (Fröhlich, 1934), indicates that compared to an elastic wet soil, the pressure in a dry, rigid soil spreads over a greater horizontal area but is more restricted in depth. This is an advantage when using a penetrometer to investigate dry buried BSC layers that are only of the order of a few millimetres thickness. Further, weakly aggregated particles propagate stress downward due to gravity. If, however, dust fills the voids between larger grains, as in the micro-layers studied here, single particles become wedged between one another. Consequently stress is propagated more horizontally (as for the footings of an arched bridge). This effect results in conical broadening of the pressure that is applied with the flat tip within the buried fossil layers. As discussed above, an active flat tip effectively becomes a shallow cone reducing its idealised vertical acuity. This has been seen in our soil proxies where the apparent width of voids appears to be slightly larger than the true width although void wall flexure will also contribute to this effect. The number of contact points for a fine grained crust is much higher than for a coarse one causing increased sliding friction. Thus, when a horizon of buried topcrust breaks the fine particles associated with it cause increased local friction on the advancing probe. For coarser dry subcrusts pressure propagation will change from a horizontal to more vertical profile until the next layer of fines is reached where the process repeats itself. An increase in vertical pressure propagation means that the probe effectively samples a thicker layer. This has been observed in both our soil proxies and buried crust soil systems. A BSC also has increased cohesion due to the existence of EPS strands cementing grains together resisting rupture resulting in higher tensional strength. This enhances horizontal pressure propagation prior to rupture and vertical pressure afterwards. Thus, asymmetry of $P'(z)$ for the EMP curves associated with BSCs is to be expected; steeper on probe entry than exit, as is observed. The

first steep peak in the spatial differential data, $P'(z)$, (Fig 9b) is considered to be representative of the physical breaking point of the first surface layer (i.e. the topcrust). Asymmetry in the amplitudes of the pre- and post- peaks is a measure of the asymmetry of the crustal $P(z)$ profile consistent with the behaviour outlined above. Asymmetry can also be enhanced by the existence of a void directly under the topcrust caused by detachment from the subcrust beneath, a pattern that has been observed in crusts in both Spain and the USA (Miralles-Mellado *et al.*, 2011; Williams et al., 2012).

4.1.2. Stability

Carbonates can be an important cementing agent in sand soils. Here it is present to a concentration of *ca.* 7.31 % in the topcrust and the concentration decreases with depth (Table A2). However, it is the size distribution not the absolute concentration of carbonate grains that mainly determines its effect on soil stability (Le Bissonnais, 1996). Thus, it is reasonable to assume the stability in fine grained regions is higher not only due to the mechanism described in the section above, but also because of the cementing of larger grains at their contact points by $CaCO_3$ precipitates in coarse grained subcrust regions. Larger uncemented carbonate grains are obviously less likely to contribute significantly to crust stability. The effect of organic matter, which in early stage cyanobacterial BSCs of the Negev is mainly comprised of EPSs, in the (buried) topcrust is manifold, especially since the presence of EPSs influences the availability and movement of water. *Colica et al.* (2014) have shown that there is a positive relationship between EPSs and water availability in BSCs. Increasing EPS content also increases soil water repellency, which in turn affects crust stability due to a reduction of water films between the grains and aggregates. Further, sand burial is likely to decrease water repellency of the soil surface, because the soil surface is repeatedly covered with new sand grains, which are not coated with organic substances of any kind. Since organic substances decrease the surface tension of the soil solution and salts tend to increase it (Holthusen *et al.*, 2012), it is likely that precipitated salts will form preferentially in larger pores with smaller specific surface areas and thus conversely organic substances will tend to be found in smaller pores with a higher specific surface area. Consequently, the mechanisms stabilising the crust

will differ between fine and coarse grained regions at the smallest scale. A higher degree of salt induced stability will occur in coarse layers and organic matter induced stability in fine grained layers. Further, as BSCs develop better in fine grained substrate (Rozenstein et al., 2014), it is reasonable to assume that coarse grained subcrust region(s) are stabilised more by inorganic mechanisms, than by cyanobacterial EPSs. However, due to the bio-physical nature of a BSC, and the physical size of microbial organisms, these organisms can also inhabit and partially block the larger soil pores adding an extra degree of subtlety to the spatial distribution of inorganic and organic material and the tortuosity of the pore space available for moisture and gaseous infiltration and percolation. Puget et al. (1995) have suggested that young and active soil organic matter has a greater effect on aggregate stability than total SOM content. However, in practice the number of microsites (contact points) that are available in the soil where EPSs can adhere and contribute to aggregate formation is limited (Molope et al., 1987). Thus, once these anchoring sites have been exhausted, the degree to which additional EPS production will contribute to stability is highly dependent on texture (Albalasmeh and Ghezzehei, 2014). In coarse-grained, sandy substrates the stabilisation curve is expected to exhibit a plateau-like shape. Rao *et al.* (2012) have demonstrated a negative correlation between the content of total carbohydrates and chlorophyll with both sand burial time and burial depth. They also show that the compressive strength (i.e. stability) decreases with sand burial depth suggesting that EPS-induced stability in buried crusts will decrease over time increasing the relative importance of other stabilising mechanisms. Our data shows that below the first few buried crusts the soil strength can vary quite considerably dependent upon burial time and history (see Figures 9 to 13). This is supported by the findings of a recent study of Kidron et al. (2016), who found that after sand burial, the risk of erosion is increased for BSCs of the Negev due to the modification (i.e. the decomposition) of their EPSs. The study of Drahorad and Felix-Henningsen (2013) has shown that it might be erroneous to determine the effect of BSCs on topsoil stability by crust removal or scraping because the main contribution to overall stability might not be due to the topcrust alone. Rather, the overall crust stability is caused by a combination of topcrust (mainly stabilised by carbonates, fines and EPSs) and subcrust (stabilised by carbonates and salts) stability (Drahorad and Felix-Henningsen, 2013).

As seen in Figure 10, the subcrust can have a higher PR compared to the overlying topcrust, necessitating complete crust removal for accurate strength analysis. But even then, the stabilising effect that the topsoil has on the complete crust (i.e. top- and subcrust combined) will not be detected or fully taken into account, potentially causing underestimation of the in-situ crust strength. Thus it is obviously preferable to study soil crust strength in multi-crust systems in-situ as in this study. In addition to methodological differences which inevitably limit the comparability of results from different studies or even groups of researchers in one study site, this finding is able to further explain the apparently contradictory results for BSC stability from study sites around the world.

4.1.3. Heat flux and dew input

The ability of heat to propagate through a material is determined by its thermal diffusivity, λ, which in turn determines its thermal response to temperature gradients. For a BSC, λ, increases with increasing C_{org} and decreasing pore volume. Therefore, the lowest thermal diffusivity of all BSC types should exist in the subcrusts of young BSCs due to lower C_{org}, and high porosity (especially if vesicular pores are abundant in the subcrust, as is the case in our crusts). After dusk and before dawn desert soils cool by radiative loss into clear skies and conductive / convective loss to the cooling planetary boundary layer compensated only by the upward flow of heat from the deep soil. This compensatory ‘warming’ of the surface by the deep soil heat flux will be frustrated by the existence of the lower thermal diffusivity of the young, low carbon (and high porosity) subcrust. Thus, it is probable that wetting by dewfall will initially be enhanced for younger crusts. Further, once formed, the dew will wick by capillarity into the less hydrophobic surface. In summary, we assume that crust burial and the resulting layering causes an increased water input via dew for the early stage crusts, helping them cope with the negative effects of the sand burial. This finding might help explain the very high frequency and large inputs of dew in the study site that have been found to be as high as 0.2 mm per event on about 200 nights per year (Heusinkveld et al., 2006; Veste et al., 2008). Further, thermal diffusivity increases disproportionately during initial wetting, the transductive profile initially increasing exponentially with low levels of moisture, which is particularly the

case for quartz rich sandsoils. This means that once the wetting process by dew has started, the surface temperature may increase above the dew point and prevent further input of dew. This latter effect will partly compensate for the increased dew input in crusts with buried subcrusts. Another effect of the burial of dark cyanobacterial BSCs by lighter quartz grains is the increased albedo and thereby decreased soil warming and soil respiration (Couradeau et al., 2016; Thomas et al., 2011).

4.1.4. Water content

Since a decreasing matrix potential changes the shape of water menisci between particles, the contracting effects of water reduction in the matrix also change during drying, at first stabilising the crust. The degree of this stabilisation depends upon the texture. While after an initial increase in stability, drying coarse grained soils will rapidly start to destabilise again, silty and clayey soils will show a much wider range of stability increase in part due to the large surface tension forces bonding finer platelet grains. This is due to the fact that in fine grained soils, the water menisci are able to transmit their tensile forces to more contact points even at low water content. In the context of the topcrust/subcrust structure of the Negev crusts, this means that coarse grained subcrust sections will be more stable than fine grained topcrust at a low pF values, whilst the topcrust is likely to be more stable at higher pF values, that is, in dry crusts. Evaporative water loss caused by near surface winds decreases with decreasing aggregate size, due to a lower abundance of secondary pores between large aggregates and therefore a higher tortuosity (i.e. a lower connectivity of the pore system). For this reason, (multiple) layering in initial crusts is likely to reduce evaporative water losses, even if only on a small scale. This also implies that the higher the number of layers, the more weakly connected and more tortuous is the pore system, consequently impeding gas diffusion through the soil matrix and reducing the hydraulic conductivity, ultimately increase surface runoff. Hence as the number of buried layers increases, we expect the evaporative losses and gaseous diffusion to decrease but dew input and surface runoff to increase. Since BSC burial by sand from the mobile dune crests is a common phenomenon at the study site, especially in the vicinity of the mobile crests and on the leeward side of the perennial shrubs where the wind speed is reduced

(Allgaier, 2008; Kidron et al., 2016), using the EMP as part of an *in-situ* water and gaseous diffusion study could provide data of ecological significance for this ecosystem. Although we are not aware of any study that quantified the distribution and spatial extent of oversanding after a sand storm in our study site, the photographs that we took in March 2013 after a sand storm (Figure A7, supplementary material) suggest that buried crusts are a very common feature in the region.

5. Conclusions

The penetrometer model and quantitative analysis presented represents a major improvement in the evaluation of PR data obtained with the EMP in comparison to the more qualitative analysis first presented by Drahorad and Felix-Henningsen (2013). By incorporating terms in the model describing shear stresses and frictional forces experienced and sampled by the penetrometer probe, crust and subcrust, the strength in biologically crusted sandsoils have been characterised numerically. Of particular note is the ability and accuracy of the model to distinguish a series of active and buried BSCs within the near surface by deconvolving the shear forces into a series of additive terms. We have demonstrated small plain tips yield high vertical and horizontal resolution resolving even weak fossil crusts whilst conical tips average PR over the height of the cone. Though a shaft diameter smaller than that of the probe reduces sliding friction it leaves the soil column unsupported which in low aggregate stability sandy soils may cause the soil to collapse after passage of the probe. As we can model the friction of plain sided probes using un-stepped shafts this has not affected the practical sensitivity of the EMP in the structural analysis of these oversanded BSC systems. This study confirms the existence *in-situ* of sub-surface fossil crust structures with lower organic carbon content and higher porosity than the healthy surface crust consistent with the *ex-situ* microscopy presented both here and in more detail elsewhere (Felde et al., 2014). The presence of fossil crusts has several consequences for the behaviour of the over sanded BSC capped sandsoils. In addition to increasing the structural rigidity of the soil (and thereby its carrying capacity, e.g. for livestock), fossil crusts are likely to influence hydrological processes such as dew input,

evaporation and infiltration. However, until detailed small-scale micrometeorological work is carried out, the environmental and ecological significance of fossil crusts to the transport processes and permeation of moisture and gases in the upper layers of these sand soils remains unknown. We have studied the response of dry oversanded BSC capped soils to point pressure applied by our flat EMP probe but not soil stability under the much higher shear forces commensurate with, for example, trampling by the hooves of animals nor the effect of increased moisture content. Soil PR response is very specific to local conditions making it difficult to relate it categorically to the effects of other soil properties (e.g. water content, texture and organic matter) as it is almost impossible to measure all of these parameters contemporaneously and non-destructively at the same spatial location (e.g. Vaz et al., 2001). Hence any attempt to generalise the absolute values determined here to other sites must be done cautiously. As we have discussed, it is likely that the mechanisms, which are stabilising the formerly mobile, single-grain structured dune sands, change in the vertical profile of the crust in relation to the number of buried topcrusts, which is why the detection of buried crusts is important for understanding these mechanisms and biologically crusted dryland soil ecology.

6. Contribution of Authors

The field and lab experiments were conducted by VJMNLF. Modelling development and analysis was undertaken by SRH. The manuscript was prepared primarily by VJMNLF, SRH and SLD with input from PFH.

7. Acknowledgements

We thank the German Research Foundation (DFG) for funding this research in the framework of the trilateral project “Biotic and abiotic factor affecting biological soil crust formation and recovery in a semiarid dune ecosystem, Gaza and NW Negev” (Project FE 218/14-2), and the Arid Ecosystems Research Center of the Hebrew University of Jerusalem. Special thanks go to Simon Berkowicz his support during field work.

8. References

Albalasmeh, A.A., Ghezzehei, T.A., 2014. Interplay between soil drying and root exudation in rhizosheath development. Plant Soil 374, 739–751. doi:10.1007/s11104-013-1910-y

Allgaier, A., 2008. Aeolian Sand Transport and Vegetation Cover, in: Breckle, S.-W., Yair, A., Veste, M. (Eds.), Arid Dune Ecosystems. Springer Berlin Heidelberg, Berlin, Heidelberg, pp. 211–224.

Almog, R., Yair, A., 2007. Negative and positive effects of topsoil biological crusts on water availability along a rainfall gradient in a sandy arid area. Catena 70, 437–442. doi:10.1016/j.catena.2006.11.012

Anderson, G., Pidgeon, J.D., Spencer, H.B., Parks, R., 1980. A NEW HAND-HELD RECORDING PENETROMETER FOR SOIL STUDIES. J. Soil Sci. 31, 279–296. doi:10.1111/j.1365-2389.1980.tb02081.x

Badorreck, A., Gerke, H.H., Hüttl, R.F., 2013. Morphology of physical soil crusts and infiltration patterns in an artificial catchment. Soil Tillage Res. 129, 1–8. doi:10.1016/j.still.2013.01.001

Belnap, J., Büdel, B., Lange, O.L., 2003. Biological Soil Crusts: Characteristics and Distribution, in: Belnap, Jayne, Lange, O.L. (Eds.), Biological Soil crusts.Structure, Function, and Management, Ecological Studies. Springer, New York, pp. 3–30.

Belnap, J., Gillette, D.A., 1998. Vulnerability of desert biological soil crusts to wind erosion: the influences of crust development, soil texture, and disturbance. J. Arid Environ. 39, 133–142.

Belnap, J., Weber, B., Büdel, B., 2016. Biological Soil Crusts as an Organizing Principle in Drylands, in: Weber, B., Büdel, B., Belnap, J. (Eds.), Biological Soil Crusts: An Organizing Principle in Drylands. Springer International Publishing, Cham, pp. 3–13. doi:10.1007/978-3-319-30214-0_1

Bengough, A.G., Mullins, C.E., 1990. Mechanical impedance to root growth: a review of experimental techniques and root growth responses. J. Soil Sci. 41, 341–358. doi:10.1111/j.1365-2389.1990.tb00070.x

Boon, N.E., Yahya, A., Kheiralla, A.F., Wee, B.S., Gew, S.K., 2005. A Tractor-mounted, Automated Soil Penetrometer–shearometer Unit for Mapping Soil Mechanical Properties. Biosyst. Eng. 90, 381–396. doi:10.1016/j.biosystemseng.2004.12.004

Büdel, B., Veste, M., 2008. Biological Crusts, in: Breckle, S.-W., Yair, A., Veste, Maik (Eds.), Arid Dune ecosystems.The Nizzana Sands in the Negev Desert. Springer, Berlin, pp. 149–155.

Chamizo, S., Rodríguez-Caballero, E., Cantón, Y., Asensio, C., Domingo, F., 2015. Penetration resistance of biological soil crusts and its dynamics after crust removal: Relationships with runoff and soil detachment. CATENA 126, 164–172. doi:10.1016/j.catena.2014.11.011

Chen, L., Rossi, F., Deng, S., Liu, Y., Wang, G., Adessi, A., De Philippis, R., 2014. Macromolecular and chemical features of the excreted extracellular polysaccharides in induced biological soil crusts of different ages. Soil Biol. Biochem. 78, 1–9. doi:10.1016/j.soilbio.2014.07.004

Colica, G., Li, H., Rossi, F., Li, D., Liu, Y., Philippis, R., 2014. Microbial secreted exopolysaccharides affect the hydrological behavior of induced biological soil crusts in desert sandy soils. Soil Biol. Biochem. 68, 62–70. doi:10.1016/j.soilbio.2013.09.017

Couradeau, E., Karaoz, U., Lim, H.C., Nunes da Rocha, U., Northen, T., Brodie, E., Garcia-Pichel, F., 2016. Bacteria increase arid-land soil surface temperature

through the production of sunscreens. Nat. Commun. 7, 10373. doi:10.1038/ncomms10373

Dexter, A.R., Czyz, E.A., Gate, O.P., 2007. A method for prediction of soil penetration resistance. Soil Tillage Res. 93, 412–419.

Dojani, S., Büdel, B., Deutschewitz, K., Weber, B., 2011. Rapid succession of Biological Soil Crusts after experimental disturbance in the Succulent Karoo, South Africa. Appl. Soil Ecol. 48, 263–269. doi:10.1016/j.apsoil.2011.04.013

Drahorad, S.L., Felix-Henningsen, P., 2013. Application of an electronic micropenetrometer to assess mechanical stability of biological soil crusts. J. Plant Nutr. Soil Sci. n/a. doi:10.1002/jpln.201200291

Drahorad, S.L., Felix-Henningsen, P., 2012. An electronic micropenetrometer (EMP) for field measurements of biological soil crust stability. J. Plant Nutr. Soil Sci. 175, 519–520. doi:10.1002/jpln.201200026

Drahorad, S.L., Felix-Henningsen, P., Eckhardt, K.-U., Leinweber, P., 2013. Spatial carbon and nitrogen distribution and organic matter characteristics of biological soil crusts in the Negev desert (Israel) along a rainfall gradient. J. Arid Environ. 94, 18–26. doi:10.1016/j.jaridenv.2013.02.006

Dümig, A., Veste, M., Hagedorn, F., Fischer, T., Lange, P., Spröte, R., Kögel-Knabner, I., 2014. Organic matter from biological soil crusts induces the initial formation of sandy temperate soils. Catena 122, 196–208. doi:10.1016/j.catena.2014.06.011

Elbert, W., Weber, B., Burrows, S., Steinkamp, J., Büdel, B., Andreae, M.O., Pöschl, U., 2012. Contribution of cryptogamic covers to the global cycles of carbon and nitrogen. Nat. Geosci. 5, 459–462. doi:10.1038/NGEO1486

Felde, V.J.M.N.L., Peth, S., Uteau-Puschmann, D., Drahorad, S., Felix-Henningsen, P., 2014. Soil microstructure as an under-explored feature of biological soil crust hydrological properties: case study from the NW Negev Desert. Biodivers. Conserv. 23, 1687–1708. doi:10.1007/s10531-014-0693-7

Fierer, N., Schimel, J.P., Holden, P.A., 2003. Influence of Drying-Rewetting Frequency on Soil Bacterial Community Structure. Microb. Ecol. 45, 63–71. doi:10.1007/s00248-002-1007-2

Fischer, T., Veste, M., Wiehe, W., Lange, P., 2010. Water repellency and pore clogging at early successional stages of microbiotic crusts on inland dunes, Brandenburg, NE Germany. CATENA 80, 47–52. doi:10.1016/j.catena.2009.08.009

Fröhlich, O.K., 1934. Druckverteilung im Baugrund. Springer, Wien.

Garcia-Pichel, F., Pringault, O., 2001. Cyanobacteria track water in desert soils. Nature 413, 380–381.

Grunwald, S., McSweeney, K., Rooney, D.J., Lowery, B., 2001. Soil layer models created with profile cone penetrometer data. Geoderma 103, 181–201. doi:10.1016/S0016-7061(01)00076-3

Guo, Y.-R., Zhao, H.-L., Zuo, X., Drake, S., Zhao, X., 2008. Biological soil crust development and its topsoil properties in the process of dune stabilization, Inner Mongolia, China. Environ. Geol. 54, 653–662.

Heusinkveld, B.G., Berkowicz, S.M., Jacobs, A.F.G., Holtslag, A.A.M., Hillen, W.C.A.M., 2006. An Automated Microlysimeter to Study Dew Formation and Evaporation in Arid and Semiarid Regions. J. Hydrometeorol. 7, 825–832. doi:10.1175/JHM523.1

Holthusen, D., Haas, C., Peth, S., Horn, R., 2012. Are standard values the best choice? A critical statement on rheological soil fluid properties viscosity and surface tension. Soil Tillage Res. 125, 61–71. doi:10.1016/j.still.2012.07.007

Hu, C., Liu, Y., Smestad Paulsen, B., Petersen, D., Klaveness, D., 2003a. Extracellular carbohydrate polymers from five desert soil algae with different cohesion in the stabilization of fine sand grain. Carbohydr. Polym. 54, 33–42. doi:10.1016/S0144-8617(03)00135-8

Hu, C., Zhang, D., Huang, Z., Liu, Y., 2003b. The vertical microdistribution of cyanobacteria and green algae within desert crusts and the development of the algal crusts. Plant Soil 257, 97–111. doi:10.1023/A:1026253307432

Jimenez Aguilar, A., Huber-Sannwald, E., Belnap, J., Smart, D.R., Arredondo Moreno, J.T., 2009. Biological soil crusts exhibit a dynamic response to seasonal rain and release from grazing with implications for soil stability. J. Arid Environ. 73, 1158–1169.

Keck, H., Felde, V.J.M.N.L., Drahorad, S.L., Felix-Henningsen, P., 2016. Biological soil crusts cause subcritical water repellency in a sand dune ecosystem located along a rainfall gradient in the NW Negev desert, Israel. J. Hydrol. Hydromech. 64. doi:10.1515/johh-2016-0001

Kidron, G.J., 2014. The negative effect of biocrusts upon annual-plant growth on sand dunes during extreme droughts. J. Hydrol. 508, 128–136. doi:10.1016/j.jhydrol.2013.10.045

Kidron, G.J., Li, X.R., Jia, R.L., Gao, Y.H., Zhang, P., 2015a. Assessment of carbon gains from biocrusts inhabiting a dunefield in the Negev Desert. Geoderma 253–254, 102–110. doi:10.1016/j.geoderma.2015.04.015

Kidron, G.J., Posmanik, R., Brunner, T., Nejidat, A., 2015b. Spatial abundance of microbial nitrogen-transforming genes and inorganic nitrogen in biocrusts along a transect of an arid sand dune in the Negev Desert. Soil Biol. Biochem. 83, 150–159. doi:10.1016/j.soilbio.2015.01.024

Kidron, G.J., Tal, S.Y., 2012. The effect of biocrusts on evaporation from sand dunes in the Negev Desert. Geoderma 179–180, 104–112. doi:10.1016/j.geoderma.2012.02.021

Kidron, G.J., Vonshak, A., Dor, I., Barinova, S., Abeliovich, A., 2010. Properties and spatial distribution of microbiotic crusts in the Negev Desert, Israel. Catena 82, 92–101.

Kidron, G.J., Yaalon, D.H., Vonshak, A., 1999. TWO CAUSES FOR RUNOFF INITIATION ON MICROBIOTIC CRUSTS: HYDROPHOBICITY AND PORE CLOGGING. Soil Sci. 164, 18–27. doi:10.1097/00010694-199901000-00004

Kidron, G.J., Yair, A., 2008. Runoff and Erosion Processes Within a Dune System, in: Breckle, S.-W., Yair, A., Veste, M. (Eds.), Arid Dune ecosystems.The Nizzana Sands in the Negev Desert. Springer, Berlin, pp. 239–249.

Kidron, G.J., Ying, W., Starinsky, A., Herzberg, M., 2016. Drought effect on biocrust resilience: High-speed winds result in crust burial and crust rupture and flaking. Sci. Total Environ. doi:10.1016/j.scitotenv.2016.11.016

Kuzyakov, Y., Blagodatskaya, E., 2015. Microbial hotspots and hot moments in soil: Concept & review. Soil Biol. Biochem. 83, 184–199. doi:10.1016/j.soilbio.2015.01.025

Lan, S., Wu, L., Zhang, D., Hu, C., 2012. Successional stages of biological soil crusts and their microstructure variability in Shapotou region (China). Environ. Earth Sci. 65, 77–88. doi:10.1007/s12665-011-1066-0

Lan, S., Zhang, Q., Wu, L., Liu, Y., Zhang, D., Hu, C., 2014. Artificially Accelerating the Reversal of Desertification: Cyanobacterial Inoculation Facilitates the Succession of Vegetation Communities. Environ. Sci. Technol. 48, 307–315. doi:10.1021/es403785j

Lapen, D.., Topp, G.., Edwards, M.., Gregorich, E.., Curnoe, W.., 2004. Combination cone penetration resistance/water content instrumentation to evaluate cone

penetration–water content relationships in tillage research. Soil Tillage Res. 79, 51–62. doi:10.1016/j.still.2004.03.023
Le Bissonnais, Y., 1996. Soil characteristics and aggregate stability, in: Soil Erosion, Conservation, and Rehabilitation. New York, pp. 41– 60.
Littmann, T., Berkowicz, S.M., 2008. The Regional Climatic Setting, in: Breckle, S.-W., Yair, A., Veste, M. (Eds.), Arid Dune ecosystems.The Nizzana Sands in the Negev Desert. Springer, Berlin, pp. 49–63.
Lowery, B., Morrison, J.E., 2002. 2.8 Soil Penetrometers and Penetrability, in: Dane, J.H., Topp, G.C. (Eds.), Methods of Soil analysis:Part 4 Physical Methods. Soil Science Society of America, Madison, Wisconsin, pp. 363–388.
Maestre, F.T., Huesca, M., Zaady, E., Bautista, S., Cortina, J., 2002. Infiltration, penetration resistance and microphytic crust composition in contrasted microsites within a Mediterranean semi-arid steppe. Soil Biol. Biochem. 34, 895–898. doi:10.1016/S0038-0717(02)00021-4
Mager, D.M., 2010. Carbohydrates in cyanobacterial soil crusts as a source of carbon in the southwest Kalahari, Botswana. Soil Biol. Biochem. 42, 313–318. doi:10.1016/j.soilbio.2009.11.009
Malam Issa, O., Défarge, C., Trichet, J., Valentin, C., Rajot, J.L., 2009. Microbiotic soil crusts in the Sahel of Western Niger and their influence on soil porosity and water dynamics. CATENA 77, 48–55. doi:10.1016/j.catena.2008.12.013
Masood, T., Mitchell, J.K., 1993. Estimation of In Situ Lateral Stresses in Soils by Cone-Penetration Test. J. Geotech. Eng. 119, 1624–1639. doi:10.1061/(ASCE)0733-9410(1993)119:10(1624)
Miralles-Mellado, I., Cantón, Y., Solé-Benet, A., 2011. Two-Dimensional Porosity of Crusted Silty Soils: Indicators of Soil Quality in Semiarid Rangelands? Soil Sci. Soc. Am. J. 75, 1330. doi:10.2136/sssaj2010.0283
Molope, M.B., Grieve, I.C., Page, E.R., 1987. Contributions by fungi and bacteria to aggregate stability of cultivated soils. J. Soil Sci. 38, 71–77. doi:10.1111/j.1365-2389.1987.tb02124.x
Nordal, S., Viggiani, G., Silva, M., Emdal, A., Paniagua, P., Andò, E., 2013. Soil deformation around a penetrating cone in silt. Géotechnique Lett. 3, 185–191. doi:10.1680/geolett.13.00067
Olsen, H.J., 1990. Construction of an electronic penetrometer for use in the field. Comput. Electron. Agric. 5, 65–75. doi:10.1016/0168-1699(90)90048-T
Persson, B.N.J., 2000. Sliding friction: Physical principles and applications, 2nd ed. ed, Nanoscience and technology. Springer, Berlin; New York.
Pócs, T., 2009. Cyanobacterial crust types, as strategies for survival in extreme habitats. Acta Bot. Hung. 51, 147–178. doi:10.1556/ABot.51.2009.1-2.16
Prasse, R., Bornkamm, R., 2000. Effect of microbiotic soil surface crusts on emergence of vascular plants. Plant Ecol. 150, 65–75.
Puget, P., Chenu, C., Balesdent, J., 1995. Total and young organic matter distributions in aggregates of silty cultivated soils. Eur. J. Soil Sci. 46, 449–459. doi:10.1111/j.1365-2389.1995.tb01341.x
Quezada, J.C., Breul, P., Saussine, G., Radjai, F., 2014. Penetration test in coarse granular material using Contact Dynamics Method. Comput. Geotech. 55, 248–253. doi:10.1016/j.compgeo.2013.09.006
Rao, B., Liu, Y., Lan, S., Wu, P., Wang, W., Li, D., 2012. Effects of sand burial stress on the early developments of cyanobacterial crusts in the field. Eur. J. Soil Biol. 48, 48–55. doi:10.1016/j.ejsobi.2011.07.009
Reynolds, J.F., Smith, D.M.S., Lambin, E.F., Turner, B.L., Mortimore, M., Batterbury, S.P.J., Downing, T.E., Dowlatabadi, H., Fernandez, R.J., Herrick, J.E., Huber-Sannwald, E., Jiang, H., Leemans, R., Lynam, T., Maestre, F.T., Ayarza, M.,

Walker, B., 2007. Global Desertification: Building a Science for Dryland Development. Science 316, 847–851. doi:10.1126/science.1131634

Rodríguez-Caballero, E., Cantón, Y., Chamizo, S., Lázaro, R., Escudero, A., 2013. Soil Loss and Runoff in Semiarid Ecosystems: A Complex Interaction Between Biological Soil Crusts, Micro-topography, and Hydrological Drivers. Ecosystems 16, 529–546. doi:10.1007/s10021-012-9626-z

Rozenstein, O., Zaady, E., Katra, I., Karnieli, A., Adamowski, J., Yizhaq, H., 2014. The effect of sand grain size on the development of cyanobacterial biocrusts. Aeolian Res. 15, 217–226. doi:10.1016/j.aeolia.2014.08.003

Russow, R., Veste, M., Böhme, F., 2005. A natural 15N approach to determine the biological fixation of atmospheric nitrogen by biological soil crusts of the Negev Desert. Rapid Commun. Mass Spectrom. 19, 3451–3456.

Sun, Y., Schulze Lammers, P., Ma, D., 2004. Evaluation of a combined penetrometer for simultaneous measurement of penetration resistance and soil water content. J. Plant Nutr. Soil Sci. 167, 745–751. doi:10.1002/jpln.200421365

Thomas, A.D., Dougill, A.J., 2007. Spatial and temporal distribution of cyanobacterial soil crusts in the Kalahari: Implications for soil surface properties. Geomorphology 85, 17–29.

Thomas, A.D., Hoon, S.R., 2010. Carbon dioxide fluxes from biologically-crusted Kalahari Sands after simulated wetting. J. Arid Environ. 74, 131–139. doi:10.1016/j.jaridenv.2009.07.005

Thomas, A.D., Hoon, S.R., Dougill, A.J., 2011. Soil respiration at five sites along the Kalahari Transect: Effects of temperature, precipitation pulses and biological soil crust cover. Geoderma 167–168, 284–294. doi:10.1016/j.geoderma.2011.07.034

Topp, G.C., Lapen, D.R., Edwards, M.J., Young, G.D., 2003. Laboratory Calibration, In-Field Validation and Use of a Soil Penetrometer Measuring Cone Resistance and Water Content. Vadose Zone J. 2, 633. doi:10.2136/vzj2003.6330

Tsoar, H., 2008. Land Use and its Effect on the Mobilization and Stabilization of the North-Western Negev Sand Dunes, in: Breckle, S.-W., Yair, A., Veste, M. (Eds.), Arid Dune ecosystems.The Nizzana Sands in the Negev Desert. Springer, Berlin, pp. 79–89.

van Herwijnen, A., Bellaire, S., Schweizer, J., 2009. Comparison of micro-structural snowpack parameters derived from penetration resistance measurements with fracture character observations from compression tests. Cold Reg. Sci. Technol. 59, 193–201. doi:10.1016/j.coldregions.2009.06.006

Vaz, C.M.P., Bassoi, L.H., Hopmans, J.W., 2001. Contribution of water content and bulk density to field soil penetration resistance as measured by a combined cone penetrometer-TDR probe. Soil Tillage Res. 60, 35–42.

Veste, M., Heusinkveld, B.G., Berkowicz, S.M., Breckle, S.-W., Littmann, T., Jacobs, A.F.G., 2008. Dew Formation and Activity of Biological Soil Crusts, in: Breckle, Siegmar-W., Yair, A., Veste, Maik (Eds.), Arid Dune Ecosystems. Springer Berlin Heidelberg, Berlin, Heidelberg, pp. 305–318.

West, N.E., 1990. Structure and Function of Microphytic Soil Crusts in Wildland Ecosystems of Arid to Semi-arid Regions 20, 179–223. doi:10.1016/S0065-2504(08)60055-0

Williams, A.J., Buck, B.J., Beyene, M.A., 2012. Biological Soil Crusts in the Mojave Desert, USA: Micromorphology and Pedogenesis. Soil Sci. Soc. Am. J. 76, 1685. doi:10.2136/sssaj2012.0021

Wilske, B., Burgheimer, J., Karnieli, A., Zaady, E., Andreae, M.O., Yakir, D., Kesselmeier, J., 2008. The CO2 exchange of biological soil crusts in a

semiarid grass-shrubland at the northern transition zone of the Negev desert, Israel. Biogeosciences 5, 1411–1423. doi:10.5194/bg-5-1411-2008

Yair, A., Almog, R., Veste, M., 2011. Differential hydrological response of biological topsoil crusts along a rainfall gradient in a sandy arid area: Northern Negev desert, Israel. Catena 87, 326–333.

Zaady, E., Offer, Z.Y., 2010. Biogenic soil crusts and soil depth: a long-term case study from the Central Negev desert highland. Sedimentology 57, 351–358.

Zhang, Y.., Wang, H.., Wang, X.., Yang, W.., Zhang, D.., 2006. The microstructure of microbiotic crust and its influence on wind erosion for a sandy soil surface in the Gurbantunggut Desert of Northwestern China. Geoderma 132, 441–449. doi:10.1016/j.geoderma.2005.06.008

Supplementary Material

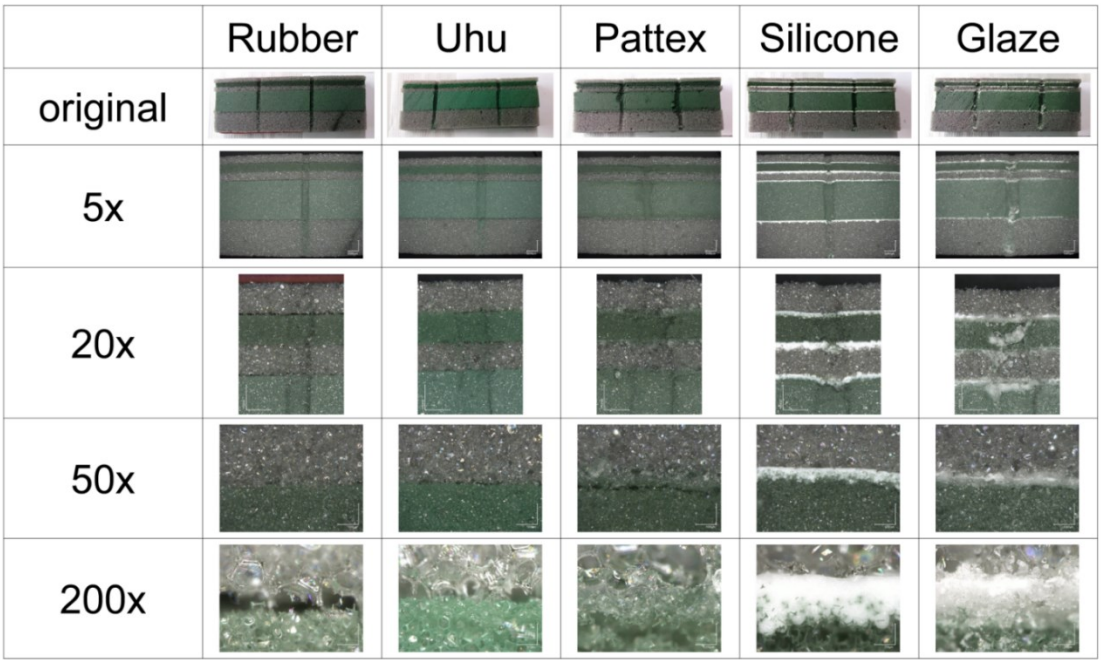

Figure A1: Microscopic images of the interfaces between layers with different bonding agents at different magnifications.

Stacks cut across penetrometer trajectory, visible in the upper three rows. Light grey and darker bands correspond to foams FF and F, respectively. The bonding methods were i) compression alone, provided by the light tension of external rubber bands, 'RU', ii) Uhu poly acrylate based glue, 'UH', iii) Pattex water based glue, 'PA', iv) sugar glaze (5 parts sugar, 1 part water), 'GL' v) commercial acetic silicone, 'SI'. Binding agents were distributed homogeneously on the layer surfaces resulting in *ca*. 0.5 mm thick penetrable coating. In the PA model soil, the bonds were denser and the glue was a more concentrated layer at the interface of the slices, which was caused by the more than 6 times higher viscosity as compared to UH (data not shown). All binding agents were allowed to dry overnight. In our experimental use of 'proxy soils', a term which we use advisably, we were not looking for a model system that has properties very similar to a natural, structured soil. Our goal was to test the model's ability of identifying boundaries between layers and evaluate the sensitivity of the penetrometer itself. For this, a homogenous, porous medium with a consistent structure and stability was much better suited. Further, the low cost and high accessibility, combined with the very high potential to manipulate the structure of the foam as necessary were the main reasons why we chose this material. Although the foam's density is much lower than that of a natural soil its performance as a test material is proof of the high sensitivity and resolution of the micropenetrometer and the ability of the mathematical model to identify buried structures.

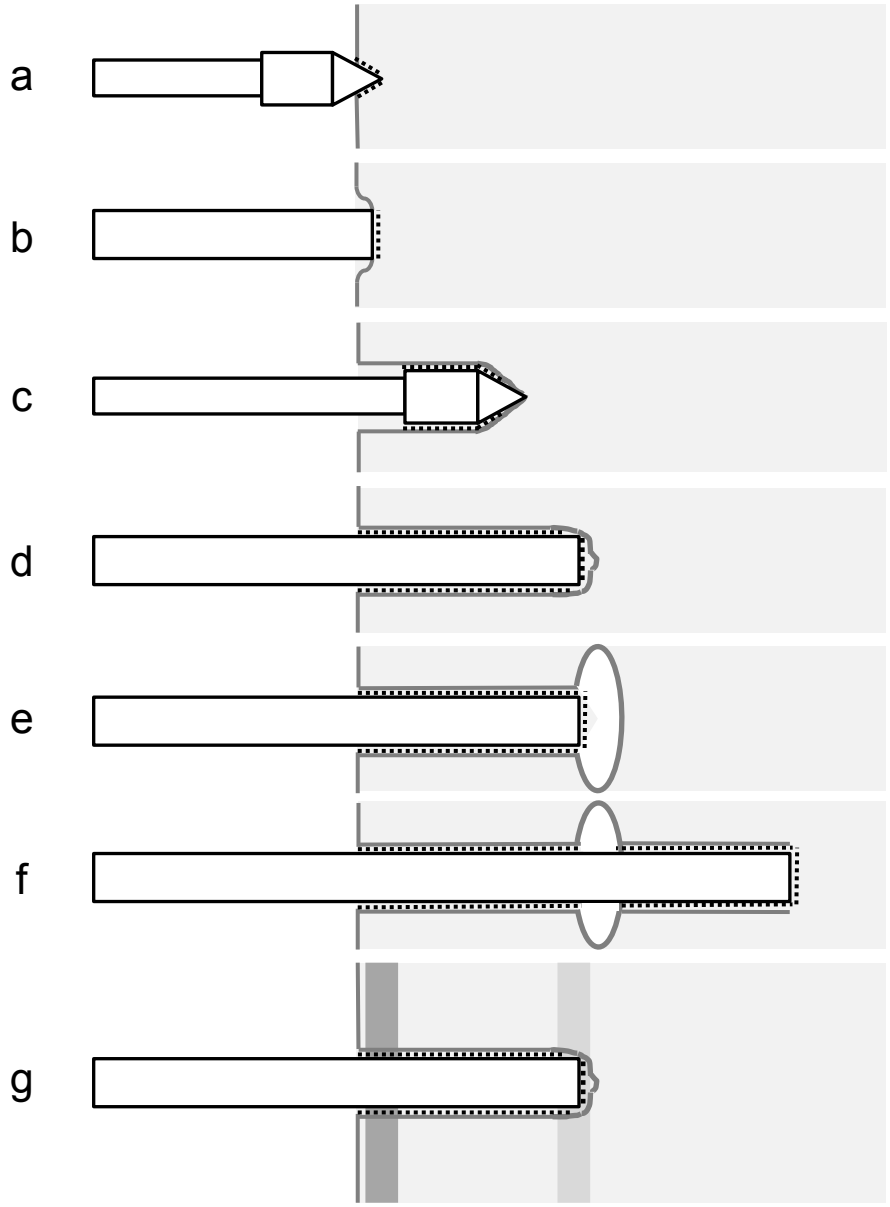

Figure A2: a) partial soil contact, conical tip, $z < H$, b) deformation around a plain faced probe, c) flow around a conical tip, stepped shaft relieves sliding friction, d) displaced material causing friction along the un-stepped shaft, plane faced probe, e) spalling of a void wall prior to penetration, f) frictional drag along an un-stepped shaft except for the void thickness. g) plain faced probe inserted through a surface BSC layer and buried horizon.

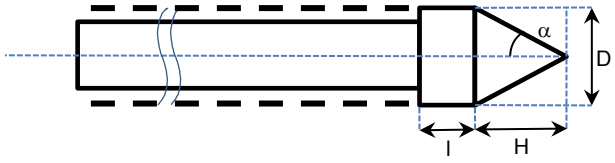

Figure A3: Bold and dotted outlines, stepped and plain shafts respectively. Conical tip angles, α, employed: 30°, 45°, 60° and (flat) 90°. Cylindrical base height, *l* = 1 mm, *D* = 3 mm. For *H*(α) see text.

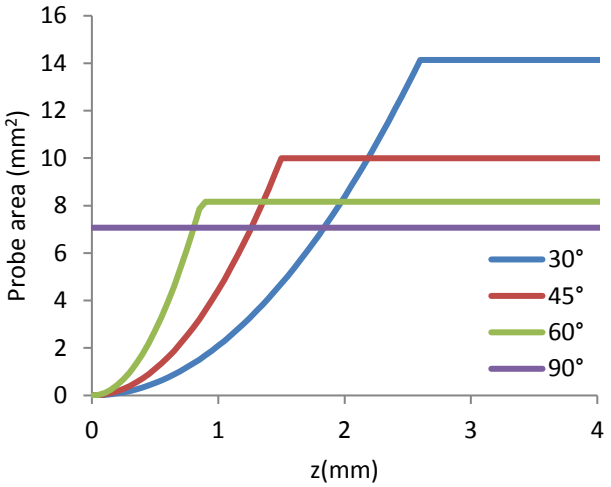

a)

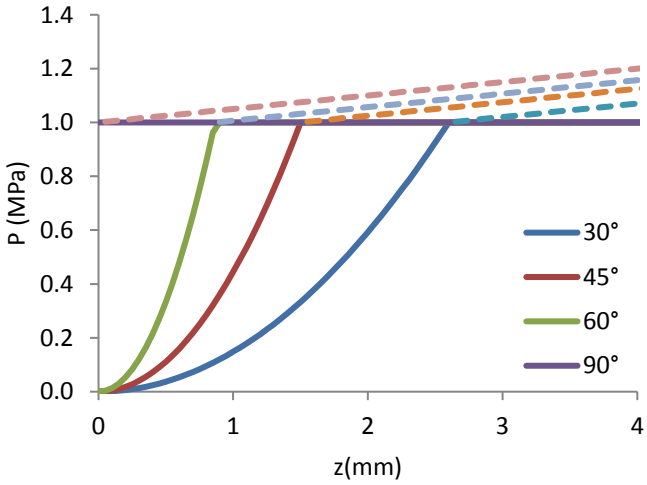

b)

Figure A4: Penetrometer modelling: a) shows the cone area in contact with the soil versus penetration depth (cone angles of 30, 45, 60 and 90°, shaft diameter 3 mm), b) displays idealized curves for initial soil penetration of conical and plain tipped probes with and without sliding friction due to drag along the shaft surface determined from equation (3.1.1). Solid curves show the pressure (σ_0= 1.0 MPa) measured by the penetrometer, and dotted, the additional pressure resulting from a soil/shaft frictional coefficient a_n = 0.05 MPa mm^{-1}.

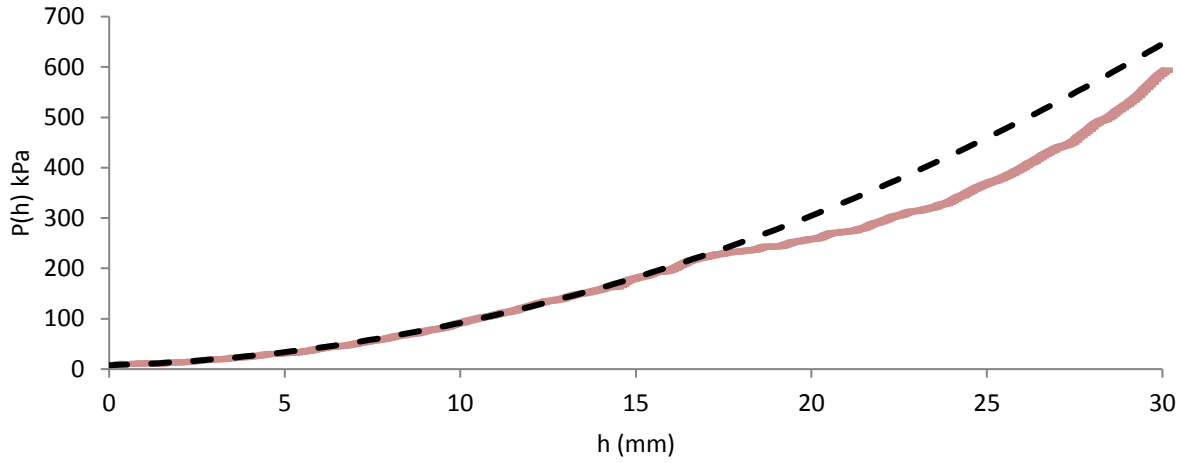

Figure A5: Second order fit using eqn. 2.5.4 to P(z) for a bare sand soil, for upper (z < 17 mm) and deeper sands (fit not shown for clarity); n = 10.

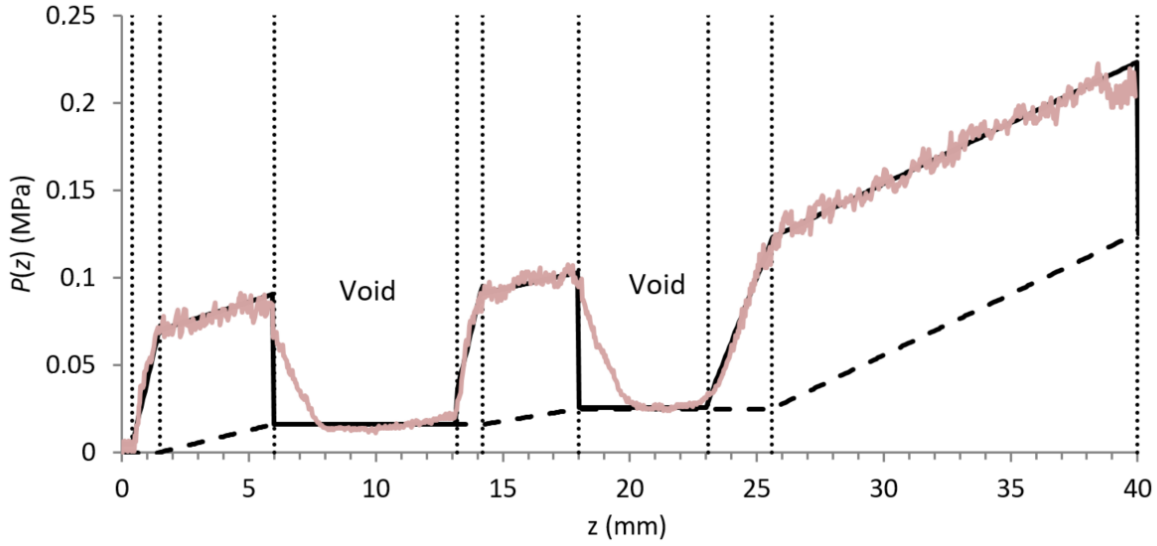

Figure A6: P(z) and model for a 3 mm plain, flat tipped probe passing perpendicularly through two approximately cylindrical voids in a homogeneous model soil, contribution from the frictional term shown dotted.

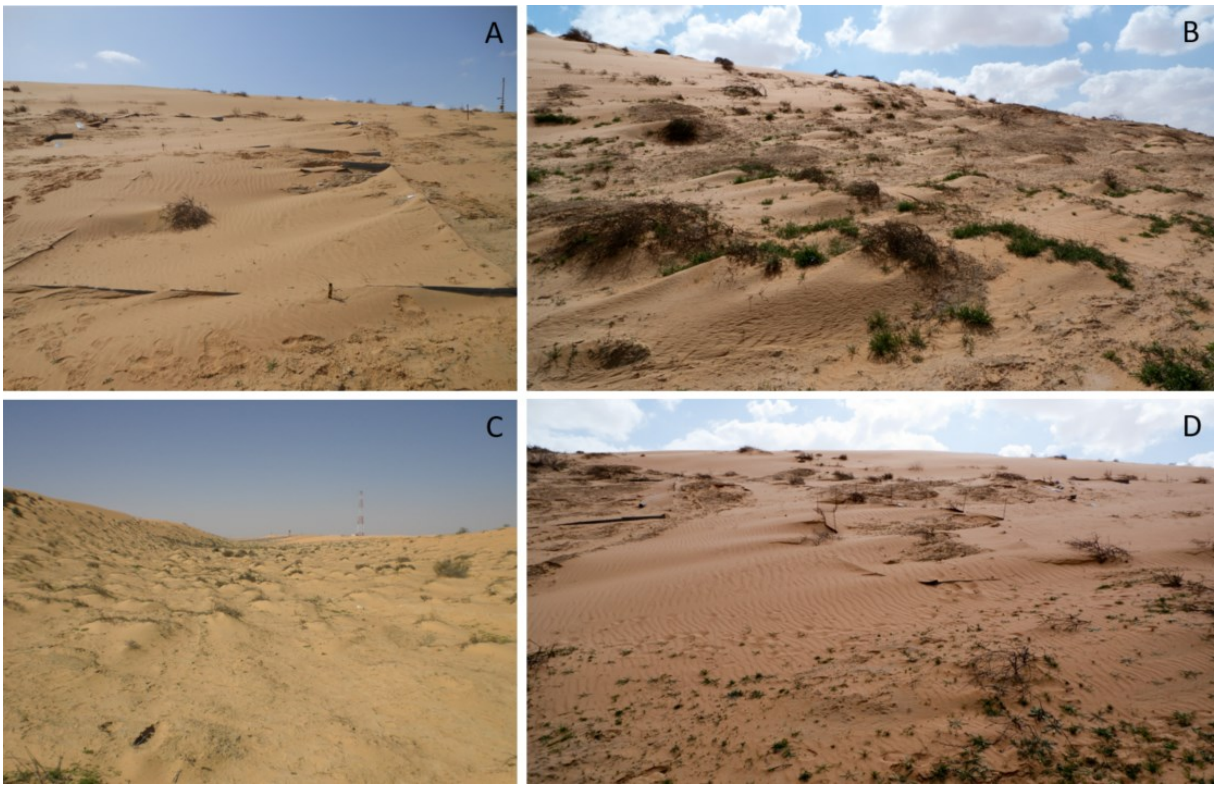

Figure A7: Photographs of buried crusts in Nizzana south (taken in March 2013). The photos A to D demonstrate that although sand burial depth and spatial distribution is different depending on slope and vegetation cover, it is a very common phenomenon after a sand storm or even high wind speeds that occur more regularly.

Table A1: Deformation stresses for the two polyurethane foams, F (foam) and FF (firm foam), respectively, as well as the four tip angles that were tested (30, 45, 60 and 90 degrees).

Proxy soil	Cone angle (°)	Stepped shafts a_n for z > 10mm (MPa mm^{-1})	Plain sided shafts a_n for z > 10mm (MPa mm^{-1})
F σ_0 = 6.2x10^{-2} MPa	30	-2.72 x10^{-4}	4.95 x10^{-3}
	45	1.67 x10^{-4}	3.73 x10^{-3}
	60	5.65 x10^{-4}	3.22 x10^{-3}
	90	6.95 x10^{-4}	4.41 x10^{-3}
FF σ_0 = 1.95x10^{-1} MPa	30	2.06 x10^{-4}	1.57 x10^{-2}
	45	2.17 x10^{-4}	1.44 x10^{-2}
	60	1.25 x10^{-3}	8.06 x10^{-3}
	90	1.95 x10^{-3}	9.08 x10^{-3}

Table A2: Soil properties for the topcrust, subcrust and topsoil in Nizzana-south (n = 3).

	C_{org} in weight-%	pH	EC in µS cm^{-1}	$CaCO_3$ in weight-%	C_{tot} in weight-%	N_{tot} in weight-%	C/N-ratio
Topcrust	0.47 (±0.12)	7.67 (±0.02)	241 (±43)	7.32 (±1.01)	1.35 (±0.10)	0.04 (±0.01)	12.96 (±4.44)
Subcrust	0.24 (±0.09)	8.40 (±0.12)	102 (±37)	5.91 (±1.58)	0.95 (±0.24)	0.02 (±0.00)	14.98 (±4.93)
Topsoil	0.18 (±0.06)	8.83 (±0.08)	69 (±9)	4.52 (±0.25)	0.72 (±0.09)	0.01 (±0.01)	23.08 (±16.83)

[November 2017 Document Ends]